Open Wilson chains for quantum impurity models: Keeping track of all bath modes

B. Bruognolo,[1,2] N.-O. Linden,[1] F. Schwarz,[1] S.-S. B. Lee,[1] K. Stadler,[1]
A. Weichselbaum,[1] M. Vojta,[3] F. B. Anders,[4] and J. von Delft[1]

[1] *Physics Department, Arnold Sommerfeld Center for Theoretical Physics and Center for NanoScience, Ludwig-Maximilians-Universität München, 80333 München, Germany*
[2] *Max-Planck-Institut für Quantenoptik, Hans-Kopfermann-Str. 1, D-85748 Garching, Germany*
[3] *Institut für Theoretische Physik, Technische Universität Dresden, 01062 Dresden, Germany*
[4] *Lehrstuhl für Theoretische Physik II, Technische Universität Dortmund, 44221 Dortmund, Germany*

When constructing a Wilson chain to represent a quantum impurity model, the effects of truncated bath modes are neglected. We show that their influence can be kept track of systematically by constructing an "open Wilson chain" in which each site is coupled to a separate effective bath of its own. This strategy enables us to cure the so-called mass-flow problem that can arise when using standard Wilson chains to treat impurity models with asymmetric bath spectral functions at finite temperature. We demonstrate this for the strongly sub-Ohmic spin-boson model at quantum criticality where we directly observe the flow towards a Gaussian critical fixed point.

arXiv:1611.05291v1 [cond-mat.str-el] 16 Nov 2016

A quantum impurity model describes a discrete set of degrees of freedom, the "impurity", coupled to a bath of excitations. For an infinite bath this is effectively an *open* system. However, the most powerful numerical methods for solving such models, Wilson's numerical renormalization group (NRG) [1, 2] and variational matrix-product-state (VMPS) generalizations thereof [3–6], actually treat it as *closed*: the continuous bath is replaced by a so-called Wilson chain, a finite-length tight-binding chain whose hopping matrix elements t_n decrease exponentially with site number n, ensuring energy-scale separation along the chain. This works well for numerous applications, ranging from transport through nanostructures [7, 8] to impurity solvers for dynamical mean-field theory [9–11]. However, replacing an open by a closed system brings about finite-size effects. Wilson himself had anticipated that the effect of bath modes neglected during discretization might need to be included perturbatively "to achieve reasonable accuracy", but concluded that "this has proven to be unnecessary" for his purposes (see p. 813 of Ref. [1]). By now, it is understood that finite-size effects often do matter. They hamper the treatment of dissipative effects [12], e.g. in the context of nonequilibrium transport [13] and equilibration after a local quench [14]. Moreover, even in equilibrium, they may cause errors when computing the bath-induced renormalization of impurity properties [15–17]. Indeed, finite-size issues constitute the arguably most serious conceptual limitation of approaches based on Wilson chains.

In this work, we set the stage for controlling finite-size effects by constructing "open Wilson chains" (OWCs) in which each site is coupled to a bath of its own, implementing energy-scale separation in a way that fully keeps track of all bath-induced dissipative and renormalization effects. The key step involved in any renormalization group (RG) approach, namely integrating out degrees of freedom at one energy scale to obtain a renormalized description at a lower scale, can then be performed more carefully than when using standard Wilson chains (SWCs). We illustrate this by focussing on renormalization effects, leaving dissipative effects for the future.

A SWC is constructed by logarithmically discretizing the bath and tridiagonalizing the resulting discrete bath Hamiltonian to obtain a tight-binding chain, with the impurity coupled to site $n = 0$ [1, 2]. Properties at temperature T are calculated using a chain of finite length N_T, chosen such its smallest energy scale matches the temperature, $t_{N_T} \simeq T$ ($k_B = 1$). However, since sites $n > N_T$ are neglected, the contribution of the corresponding truncated bath modes (TBMs) to the renormalization of impurity properties is missing [17]. For example, for a local level linearly coupled to a bath with an asymmetric bath spectrum, this coupling generates a physical shift in the level energy. When this shift is computed using a SWC of length N_T, the result contains a temperature-dependent error. Hence, the use of SWCs generically leads to qualitative errors in the temperature dependence of renormalized model parameters, called the "mass-flow problem" [16, 17]. Quantitative errors persist even for $T \to 0$, when $N_T \to \infty$, because constructing a SWC actually involves neglecting TBMs at *every* site.

The mass-flow problem is particularly serious when targeting a quantum critical point, where it causes errors for critical exponents describing finite-temperature properties at the critical point. This has been studied in some detail for the dissipative harmonic oscillator (DHM) and the sub-Ohmic spin-boson model (SBM). For both, SWCs are unable to even qualitatively describe the temperature dependence of the local susceptibility, $\chi(T)$, at criticality [15–17]. Both involve Gaussian criticality of ϕ^4 type and hence a bosonic mode whose excitation energy vanishes at the critical fixed point. The finite-T RG flow in its vicinity cannot be correctly described using finite-length SWCs because the erroneous mass dominates over physical interaction effects. Summarizing, methods based on SWCs produce systematic quantitative errors for all impurity problems with asymmetric baths, and they fail even qualitatively in addressing Gaussian criticality and other phenomena with zero modes.

Here we show that these issues *can* be addressed using

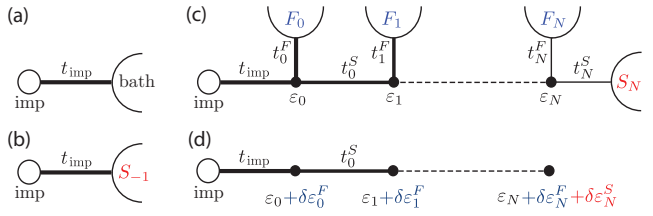

Figure 1. (a) Impurity model. (b) Initialization. (c) Open Wilson chain (OWC). (d) Renormalized Wilson chain (RWC).

OWCs: The bath coupled to each site of the OWC induces an energy shift for that site that can be computed *exactly* and used to define a "renormalized Wilson chain" (RWC). The ground-state properties of a RWC of length N_T mimic the finite-T properties of the original model in a way that is free from mass-flow problems. We demonstrate this explicitly by using VMPS techniques [6] on RWCs to compute $\chi(T)$ for the DHO and SBM. We also compute the energy-level flow of the SBM; it unambiguously reveals flow towards a Gaussian fixed point with a dangerously irrelevant interaction term.

Model.— We consider a generic single-band impurity model with Hamiltonian $\mathcal{H} = \mathcal{H}^{\rm imp}[b^\dagger t_{\rm imp}] + \mathcal{H}^{\rm bath}$, where $\mathcal{H}^{\rm bath}$ describes the bath, and $\mathcal{H}^{\rm imp}$ the impurity and its coupling to the bath via normalized bath operators $b^\dagger$ and b, with coupling constant $t_{\rm imp}$ [Fig. 1(a)]. The free ($t_{\rm imp}=0$) dynamics of $b^\dagger$, generated by $\mathcal{H}^{\rm bath}$, is encoded in the free retarded correlator $\mathcal{G}^{\rm bath}(\omega) = \langle\langle b|b^\dagger\rangle\rangle_\omega$, which is uniquely characterized by its spectral function $\mathcal{A}^{\rm bath}(\omega) = -\frac{1}{\pi}{\rm Im}\,\mathcal{G}^{\rm bath}(\omega)$. The impurity dynamics is therefore fully determined once $\mathcal{H}^{\rm imp}$ and the "bath spectrum", $\Gamma^{\rm bath}(\omega) = |t_{\rm imp}|^2\mathcal{A}^{\rm bath}(\omega)$, have been specified.

Continued-fraction expansion.— One well-known way of mapping an impurity model to a chain is to iteratively construct a continued-fraction expansion (CFE) for $\mathcal{G}^{\rm bath}$ [18]. Our main new idea is to do this in a way that *zooms in on low energies* without discarding high-energy information. Our construction involves a sequence of retarded correlators $\mathcal{G}_n^X(\omega)$, with $X = S$ or F, describing the effective "slow" (low-energy) or "fast" (high-energy) bath modes of iteration step n, with spectral functions $\mathcal{A}_n^X(\omega) = -\frac{1}{\pi}{\rm Im}\,\mathcal{G}_n^X(\omega)$ having unit weight, $\int d\omega \mathcal{A}_n^X(\omega) = 1$. We initialize our CFE construction with $\mathcal{G}_{-1}^S = \mathcal{G}^{\rm bath}$ [Fig. 1(b)]. Starting with $n=0$, we iteratively use $\mathcal{G}_{n-1}^S$, describing the low-energy modes of the previous iteration, as input to define a new retarded correlator $\mathcal{G}_n$ and its retarded self-energy Σ_n,

$$\mathcal{G}_n(\omega) = \mathcal{G}_{n-1}^S(\omega) = 1/\left[\omega - \varepsilon_n - \Sigma_n(\omega)\right], \qquad (1)$$

with $\varepsilon_n = \int d\omega\, \omega \mathcal{A}_n(\omega)$ [19]. Then we split this self-energy into low- and high-energy parts by writing it as

$$\Sigma_n(\omega) = \Sigma_n^S(\omega) + \Sigma_n^F(\omega), \quad \Sigma_n^X(\omega) = |t_n^X|^2\mathcal{G}_n^X(\omega). \quad (2)$$

Here the corresponding retarded correlators $\mathcal{G}_n^{S/F}$ are defined by choosing their rescaled spectral functions $|t_n^{S/F}|^2\mathcal{A}_n^{S/F}$ to represent the low- and high-energy parts of $-\frac{1}{\pi}{\rm Im}\Sigma_n$, with t_n^X chosen such that $\mathcal{A}_n^X$ has unit weight [see S-1 A of [19] for details]. Iterating, using $\mathcal{G}_n^S$ as input to compute new correlators $\mathcal{G}_{n+1}^X$ while retaining the self-energy Σ_n^F, we obtain a sequence of exact CFE representations for $\mathcal{G}^{\rm bath}$. That of depth 2, e.g., reads

$$\mathcal{G}^{\rm bath}(\omega) = \cfrac{1}{\omega - \varepsilon_0 - \Sigma_0^F(\omega) - \cfrac{|t_0^S|^2}{\omega - \varepsilon_1 - \Sigma_1^F(\omega) - \cfrac{|t_1^S|^2}{\omega - \varepsilon_2 - \Sigma_2(\omega)}}}.$$

To ensure energy-scale separation, we choose $\mathcal{A}_n^X(\omega)$ such that the CFE parameters decrease montonically, $\max\{|\varepsilon_n|, |t_n^S|\} \leqslant \max\{|\varepsilon_{n-1}|, |t_{n-1}^S|\}/\Lambda$, with $\Lambda > 1$ [20].

Open Wilson chain.— We now use the CFE data $(\varepsilon_n, t_n^X, \mathcal{G}_n^X)$ to represent the original bath in terms of a chain with $N+1$ sites, each coupled to a bath of its own, and site 0 coupled to the impurity (site -1) [Fig. 1(c)]. This OWC is constructed such that the free ($t_{\rm imp} = 0$) correlator of site 0 is exactly equal to the depth-N CFE found above, i.e. $\mathcal{G}_0 = \mathcal{G}^{\rm bath}$, implying that the chain and original bath have the same effect on the impurity.

The key point is that each CFE step of writing $\mathcal{G}_{n-1}^S(\omega)$ in the form $\mathcal{G}_n(\omega) = 1/[\omega - \varepsilon_n - \Sigma_n(\omega)]$ can be implemented on the level of the Hamiltonian: it corresponds to replacing the bath represented by $\mathcal{G}_{n-1}^S$, say S_{n-1}, by a new site n, with energy ε_n and normalized site operators $f_n^\dagger$ and f_n, which is linearly coupled to a new bath that generates the self-energy Σ_n. In the present case, the latter is split into low- and high-energy contributions, $\Sigma_n^S + \Sigma_n^F$. We can generate these by linearly coupling the new site with couplings t_n^S and t_n^F to *two* new baths, say S_n and F_n, via normalized bath operators $b_{Sn}^\dagger$, b_{Sn} and $b_{Fn}^\dagger$, b_{Fn}, that are governed by bath Hamiltonians $\mathcal{H}_n^X$ chosen such that $\langle\langle b_{Xn}|b_{Xn}^\dagger\rangle\rangle_\omega$ equals the $\mathcal{G}_n^X(\omega)$ found above [see S-1 A of [19] for details]. For the next iteration, we retain the fast bath F_n, but replace the slow bath S_n by a new site $n+1$ coupled to new baths S_{n+1} and F_{n+1}, etc. This leads to replacing $\mathcal{H}$ by $\mathcal{H}_N^{\rm OWC} = \mathcal{H}_N^{\rm SWC} + \mathcal{H}_N^{\rm TBM}$, with

$$\begin{aligned}
\mathcal{H}_N^{\rm SWC} &= \mathcal{H}_f^{\rm imp} + \sum_{n=0}^{N} \varepsilon_n f_n^\dagger f_n + \sum_{n=0}^{N-1} (f_{n+1}^\dagger t_n^S f_n + {\rm H.c.}),\\
\mathcal{H}_N^{\rm TBM} &= \sum_{n=0}^{N} (b_{Fn}^\dagger t_n^F f_n + {\rm H.c.}) + \sum_{n=0}^{N} \mathcal{H}_n^F \\
&\quad + (b_{SN}^\dagger t_N^S f_N + {\rm H.c.}) + \mathcal{H}_N^S\,,
\end{aligned} \qquad (3)$$

and $\mathcal{H}_f^{\rm imp} = \mathcal{H}^{\rm imp}[f_0^\dagger\, t_{\rm imp}]$. This chain Hamiltonian is depicted schematically in Fig. 1(c). $\mathcal{H}_N^{\rm SWC}$ has the structure of a SWC, while $\mathcal{H}_N^{\rm TBM}$ describes the couplings to all fast baths $F_{n\leqslant N}$, and of the last site N to its slow bath S_N. These "fast and last slow" baths F_n and S_N constitute TBMs, since a SWC neglects them. By instead using an OWC, we can keep track of their influence, namely to shift, mix and broaden the eigenstates of those subchains to which they couple.

Renormalized Wilson chain.— For concrete numerical calculations, we need to approximate an OWC by a RWC

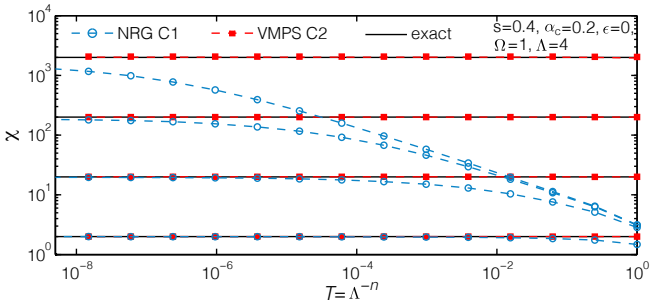

Figure 2. DHO susceptibility $\chi(T)$ as function of temperature, computed by NRG on C1-RWCs (circles) and by VMPS on C2-RWCs (squares), for $\alpha = 0.1, 0.19, 0.199, 0.1999$ (from bottom to top). Solid lines show exact results.

that can be treated using standard NRG or VMPS methods, while still including information about the TBMs. To this end, we replace $\mathcal{H}^{\rm OWC}$ by $\mathcal{H}^{\rm RWC}$ [Fig. 1(e)], a Hamiltonian of the same form as $\mathcal{H}^{\rm SWC}$ (without fast or last baths), but with each onsite energy ε_n shifted to

$$\tilde{\varepsilon}_n = \varepsilon_n + \delta\varepsilon_n^F + \delta_{nN}\,\delta\varepsilon_N^S\,, \quad \delta\varepsilon_n^X = {\rm Re}\big[\Sigma_n^X(0)\big]. \qquad (4)$$

For the CFE of $\mathcal{G}^{\rm bath} = \mathcal{G}^S_{-1} = \mathcal{G}_0$, this amounts to replacing the slow and fast self-energies by the real parts of their zero-frequency values [21]. Therefore ${\rm Re}[\Sigma^{\rm bath}(0)]$, the real part of the zero-frequency self-energy of $\mathcal{G}^{\rm bath}$, is reproduced correctly [22], irrespective of the length N of the RWC used to calculate $\mathcal{G}^{\rm bath}$. (Since the imaginary parts of all self-energies are neglected, dissipative effects are not included.) If the original bath spectrum is symmetric, $\Gamma^{\rm bath}(\omega) = \Gamma^{\rm bath}(-\omega)$, as often happens for fermionic models, then $\delta\varepsilon_n^{S/F} = 0$. However for an asymmetric bath function [e.g. $\Gamma^{\rm bath}(\omega<0)=0$, as is the case for bosonic baths], these shifts are in general nonzero.

We will henceforth consider two types of RWCs, labelled by C1 or C2 [23]. A C1 chain includes only fast shifts ($\delta\varepsilon_N^S = 0$); this turns out to lead to results qualitatively similar to those obtained using a SWC constructed by discretizing the bath S_{-1} logarithmically à la Wilson and tridiagonalizing the bath Hamiltonian $\mathcal{H}^S_{-1}$. A C2 chain includes both the fast and slow shifts from Eq. (4), thus correctly reproducing ${\rm Re}[\Sigma^{\rm bath}(0)]$.

Dissipative harmonic oscillator.— As a first example, consider a DHO with Hamiltonian $\mathcal{H}^{\rm imp}_{\rm DHO} + \mathcal{H}^{\rm bath}$, where

$$\mathcal{H}^{\rm imp}_{\rm DHO} = \Omega a^\dagger a + \tfrac{1}{2}(a+a^\dagger)\big[\epsilon + t_{\rm imp}(b\ \ + b^\dagger)\big] \qquad (5)$$

describes an "impurity" oscillator with bare frequency Ω and displacement force ϵ, linearly coupled to a bosonic bath. The bath spectral function has the form

$$\Gamma^{\rm bath}(\omega) = 2\alpha\omega_{\rm c}^{1-s}\omega^s, \quad 0<\omega<\omega_{\rm c}\,, \qquad (6)$$

where $s > -1$, α characterizes the dissipation strength and $\omega_{\rm c}$ is a cutoff frequency, henceforth set to unity. This model is exactly solvable. The static impurity susceptibility at temperature T, defined by $\chi(T) = \frac{d\langle a+a^\dagger\rangle_T}{d\epsilon}|_{\epsilon=0}$, turns out to be temperature-independent and given by [17] $\chi_{\rm exact}(T) = 1/\Omega_{\rm r}$, where $\Omega_r = \Omega + {\rm Re}[\mathcal{G}^{\rm bath}(\omega=0)]$ can be interpreted as renormalized impurity frequency, reduced relative to the bare one by the coupling to the bath. It vanishes at the critical coupling $\alpha_{\rm c} = s\Omega/(2\omega_{\rm c})$, beyond which the model becomes unstable.

When $\chi(T)$ is computed numerically for $\alpha<\alpha_{\rm c}$ using NRG to perform thermal averages on SWCs of length N_T, one does not obtain a constant but a temperature-dependent curve [15–17]. We find the same using NRG on C1-RWCs of length N_T (Fig. 2, circles). The reason is the neglect of the TBMs associated with sites $n > N_T$: their contribution to the renormalization shift ${\rm Re}[\mathcal{G}^{\rm bath}(\omega=0)]$ in $\Omega_{\rm r}$ is missing. The approach developed above offers a straightforward cure: we simply compute $\chi(T)$ using C2-RWCs of length N_T, thus incorporating the energy shift induced by the remaining TBMs via the slow-mode shift for site N_T. Since the latter substantially affects the low-energy spectrum, these calculations require VMPS methods (see S-2 B and S-2 C of [19] for details). They yield T-independent χ values (Fig. 2, squares) in excellent agreement with the exact ones (Fig. 2, solid lines).

We remark that SWCs constructed using previous discretization schemes [24–26] either strongly over- or underestimate the critical coupling $\alpha_{\rm c}$, reflecting the presence of discretization artefacts. In contrast, our C2-RWCs yield $\alpha_{\rm c}$ values that match the analytic results almost perfectly (see S-3 D of [19]). Thus, our RWC construction constitutes a general new discretization scheme free of the discretization artefacts of previous schemes.

Spin-boson model.— Next we consider the SBM, which is not exactly solvable. In its Hamiltonian $\mathcal{H}^{\rm imp}_{\rm SBM} + \mathcal{H}^{\rm bath}$,

$$\mathcal{H}^{\rm imp}_{\rm SBM} = -\tfrac{1}{2}\Delta\hat{\sigma}_x + \tfrac{1}{2}\hat{\sigma}_z\big[\epsilon + t_{\rm imp}(b+b^\dagger)\big] \qquad (7)$$

describes a spin-$\frac{1}{2}$ "impurity" ($\hat{\sigma}_i$ being Pauli matrices) linearly coupled to a bosonic bath, with $\Gamma^{\rm bath}(\omega)$ again given by Eq. (6). ϵ and Δ denote the bias and the tunnel splitting of the impurity spin, respectively.

For the *sub-Ohmic* case ($0<s<1$), increasing α at zero temperature drives the SBM through a quantum phase transition (QPT) from a delocalized to a localized phase (with $\langle\hat{\sigma}_z\rangle_0 = 0$ or $\neq 0$, respectively). According to a quantum-to-classical correspondence (QCC) argument [15, 16, 27], this QPT belongs to the same universality class as that of a classical 1D Ising chain with long-ranged interactions [28]. Thus, the critical exponents characterizing the QPT follow mean-field predictions for $s \leqslant 0.5$ and obey hyperscaling for $0.5 < s < 1$. The QCC predictions were confirmed numerically using Monte Carlo methods [29] or sparse polynomial bases [30].

In contrast, verifying the QCC predictions using NRG turned out to be challenging. Initial NRG studies [15] yielded non-mean-field exponents for $s<0.5$, but were subsequently [16, 17] found to be unreliable, due to two inherent limitations of NRG. The first was a too severe NRG truncation of Hilbert space in the localized phase; it was overcome in Ref. [6] by using a VMPS approach

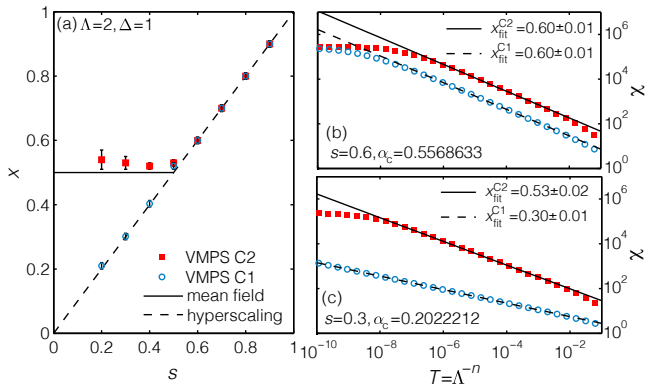

Figure 3. (a) Critical exponent x for the sub-Ohmic SBM, as function of s, computed by VMPS using RWCs of type C1 (circles) and C2 (squares). Examples of $\chi(T)$ curves used to extract these exponents are shown in (b) for $s = 0.3$ and (c) for $s = 0.6$. Error bars in (a) reflect the effect of varying the fitting range in plots like (b) and (c).

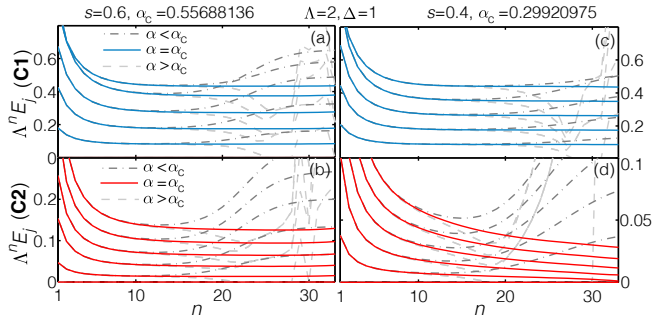

Figure 4. Energy-level flow diagrams for the sub-Ohmic SBM with $s = 0.6$ (left column) and $s = 0.4$ (right column), computed by VMPS techniques [5, 19] on C1-RWCs (top row) and C2-RWCs (bottom row). Dashed lines depict flow to delocalized ($\alpha < \alpha_c$) or localized fixed points ($\alpha > \alpha_c$), solid lines depict critical flow ($\alpha = \alpha_c$). For the latter, the C2 flow in (d) is characteristic of a Gaussian fixed point.

involving an optimized boson basis [31–33] on a SWC, which reproduced QCC predictions for critical exponents characterizing zero-temperature behavior. The second NRG limitation was the mass-flow problem: for exponents describing *finite*-temperature critical behavior at $\alpha = \alpha_c$, it causes NRG on SWCs to yield hyperscaling results not only for $0.5 < s < 1$ (correct) but also for $s < 0.5$ (incorrect). For example, consider the susceptibility $\chi(T) = \frac{d\langle\hat{\sigma}_z\rangle_T}{d\epsilon}|_{\epsilon=0}$, which scales as $\chi(T) \propto T^{-x}$ at the critical coupling α_c. The QCC predicts $x = 0.5$ for $s < 0.5$ and $x = s$ for $0.5 < s < 1$. In contrast, past NRG calculations yielded $x = s$ throughout the interval $0 < s < 1$ [16, 17, 24]. We recover the latter behavior if we compute $\chi(T)$ via VMPS calculations on length-N_T C1-RWCs [Fig. 3(a), circles]. In contrast, if we use length-N_T C2-RWCs instead, the results for x [Fig. 3(a), squares] agree well with QCC predictions, showing that the mass-flow problem has been cured.

Critical energy-level flow diagrams.— The reason why the sub-Ohmic SBM shows qualitatively different critical behavior for $0.5 < s < 1$ and $s \leqslant 0.5$ is that the critical fixed point is interacting for the former but Gaussian for the latter [17]. To elucidate the difference, Fig. 4 shows energy-level flow diagrams, obtained by plotting the rescaled lowest-lying energy eigenvalues of length-N Wilson chains, $\Lambda^N E_j$, as functions of N. For $s = 0.6$ (left column), having an interacting critical fixed point for which mass-flow effects are not relevant, the critical level flows for RWCs of type C1 and C2 are qualitatively similar [Figs. 4(a,b)], becoming stationary (N-independent) for large N, in a manner familiar from fermionic NRG.

In contrast, for $s = 0.4$ (right column), having a Gaussian fixed point for which mass-flow effects do matter, the critical C1 and C2 level flows are very different: whereas the C1 flow becomes stationary [Fig. 4(c)] (an artefact of neglecting slow-mode shifts), the low-lying C2 levels all flow towards zero [Fig. 4(d)], causing the level spacing to decrease towards zero, too. This striking behavior, inaccessible when using SWCs, is characteristic of a Gaussian fixed point: it implies that the fixed-point excitation spectrum contains a zero-energy bosonic mode. Remarkably, our C2-RWCs yield a *quantitatively* correct description of the critical spectral flow for $0 < s < 0.5$: it follows a power law $\Lambda^n E_j \propto \varepsilon_n^\kappa$ with $\kappa = (2s-1)/3$, in perfect agreement with the prediction from controlled perturbative RG for a ϕ^4-type theory with a dangerously irrelevant quartic coupling (see S-4 D of [19]).

Conclusions and outlook.— Open Wilson chains are representations of quantum impurity models that achieve energy-scale separation while fully keeping track of the effects of bath modes, by iteratively replacing them by a sequence of separate baths at successively lower energy scales, one for each chain site. This sets the stage for systematically including the effects of these baths. We have taken the first step in that direction, using the bath-induced energy shift for each site to define a renormalized Wilson chain. Remarkably, this simple scheme is sufficiently accurate to yield renormalized impurity properties free from the long-standing mass flow problem. The next step, namely integrating out each site's bath more carefully, should lead to a description of dissipative effects on Wilson chains, as required for nonequilibrium situations. For example, the effect of bath F_n on the eigenstates of a length-n subchain could be treated using some simple approximation capable of mixing and broadening the eigenlevels (e.g. an equation-of-motion approach with a decoupling scheme). This is left for future work.

Finally, we note that our iterative construction of renormalized Wilson chains constitutes a well-controlled new discretization scheme that offers progress on two further fronts, unrelated to finite-size effects but relevant, e.g., when using NRG as impurity solver for dynamical mean field theory [9–11], or to study multi-impurity models [34]. First, it avoids the discretization artefacts known to arise when conventional schemes [1, 24–26] are used to treat strongly asymmetric bath spectra. And second, it can be generalized straightforwardly to treat multi-flavor models having nondiagonal bath spectral functions (see S-1 B of [19]).

Acknowledgments.— We thank Andrew Mitchell for a stimulating discussion on discretizing multiflavor impurity models. This research was supported by the DFG through the Excellence Cluster "Nanosystems Initiative Munich", SFB/TR 12, SFB 631, SFB 1143 (M.V.), AN 275/8-1 (F.B.A), and WE4819/2-1 (A.W.).

[1] K. G. Wilson, Rev. Mod. Phys. **47**, 773 (1975).
[2] R. Bulla, T. A. Costi, and T. Pruschke, Rev. Mod. Phys. **80**, 395 (2008).
[3] H. Saberi, A. Weichselbaum, and J. von Delft, Phys. Rev. B **78**, 035124 (2008).
[4] A. Weichselbaum, F. Verstraete, U. Schollwöck, J. I. Cirac, and J. von Delft, Phys. Rev. B **80**, 165117 (2009).
[5] I. Pizorn and F. Verstraete, Phys. Rev. Lett. **108**, 067202 (2012).
[6] C. Guo, A. Weichselbaum, J. von Delft, and M. Vojta, Phys. Rev. Lett. **108**, 160401 (2012); B. Bruognolo, A. Weichselbaum, C. Guo, J. von Delft, I. Schneider, and M. Vojta, Phys. Rev. B **90**, 245130 (2014).
[7] L. Borda, G. Zaránd, W. Hofstetter, B. I. Halperin, and J. von Delft, Phys. Rev. Lett. **90**, 026602 (2003).
[8] A. V. Kretinin, H. Shtrikman, D. Goldhaber-Gordon, M. Hanl, A. Weichselbaum, J. von Delft, T. A. Costi, and D. Mahalu, Phys. Rev. B **84**, 245316 (2011).
[9] R. Bulla, Phys. Rev. Lett. **83**, 136 (1999).
[10] T. Pruschke and R. Bulla, Eur. Phys. J. B **44** (2005).
[11] K. M. Stadler, Z. P. Yin, J. von Delft, G. Kotliar, and A. Weichselbaum, Phys. Rev. Lett. **115**, 136401 (2015).
[12] A. Rosch, Eur. Phys. J. B **85**, 6 (2012).
[13] F. B. Anders, J. Phys.: Condens. Matter **20**, 195216 (2008).
[14] F. B. Anders and A. Schiller, Phys. Rev. Lett. **95**, 196801 (2005); H. E. Türeci, M. Hanl, M. Claassen, A. Weichselbaum, T. Hecht, B. Braunecker, A. Govorov, L. Glazman, A. İmamoğlu, and J. von Delft, Phys. Rev. Lett. **106**, 107402 (2011); C. Latta, F. Haupt, M. Hanl, A. Weichselbaum, M. Claassen, P. Fallahi, S. Faelt, L. Glazman, J. von Delft, H. E. Türeci, and A. İmamoğlu, Nature **474**, 627 (2011).
[15] M. Vojta, N.-H. Tong, and R. Bulla, Phys. Rev. Lett. **94**, 070604 (2005).
[16] M. Vojta, N.-H. Tong, and R. Bulla, Phys. Rev. Lett. **102**, 249904 (2009).
[17] M. Vojta, R. Bulla, F. Güttge, and F. Anders, Phys. Rev. B **81**, 075122 (2010).
[18] G. Grosso and G. P. Parravicini, Adv. Chem. Phys. **62** (1985); M. Foulkes and R. Haydock, J. Phys. C: Solid State Phys. **19**, 6573 (1986); E. R. Gagliano and C. A. Balseiro, Phys. Rev. Lett. **59**, 2999 (1987); Q. Si, M. J. Rozenberg, G. Kotliar, and A. E. Ruckenstein, Phys. Rev. Lett. **72**, 2761 (1994); K. A. Hallberg, **52**, 9827(R) (1995).
[19] See Supplementary Material at [url], which includes Refs. [35–41], for details about the OWC construction, numerical methods used and additional numerical data.
[20] If $\Gamma^{\rm bath}(\omega)$ has power-law form, $\propto\omega^s$, we can achieve this by taking the support of $\mathcal{A}_n^S$ and $\mathcal{A}_n^F$ to *partition* that of $-\frac{1}{\pi}\mathrm{Im}\,\Sigma_n$ into low- and high-energy regimes [19].
[21] This choice of $\delta\varepsilon_n^X$ aims to correctly describe low-energy properties, in order to solve the mass-flow problem. More generally, the $\delta\varepsilon_n^X$ may be viewed as fit parameters that optimize the truncated CFE representation of $\mathcal{G}^{\rm bath}(\omega)$.
[22] For the single-impurity Anderson model, this guarantees that the height of the zero-temperature Kondo resonance at $\omega = 0$, which is governed solely by $\mathrm{Re}[\Sigma^{\rm bath}(0)]$, is reproduced correctly, irrespective of the choice of Λ.
[23] Chains that include neither fast nor slow shifts, $\delta\varepsilon_n^{F,S} = 0$, yield completely incorrect results, see S-3 of [19].
[24] R. Bulla, N.-H. Tong, and M. Vojta, Phys. Rev. Lett. **91**, 170601 (2003); R. Bulla, H.-J. Lee, N.-H. Tong, and M. Vojta, Phys. Rev. B **71**, 045122 (2005).
[25] J. Vivaldo L. Campo and L. N. Oliveira, Phys. Rev. B **72**, 104432 (2005).
[26] R. Žitko and T. Pruschke, Phys. Rev. B **79**, 085106 (2009).
[27] M. Vojta, Phys. Rev. B **85**, 115113 (2012).
[28] M. E. Fisher, S.-k. Ma, and B. G. Nickel, Phys. Rev. Lett. **29**, 917 (1972); E. Luijten and H. W. J. Blöte, Phys. Rev. B **56**, 8945 (1997).
[29] A. Winter, H. Rieger, M. Vojta, and R. Bulla, Phys. Rev. Lett. **102**, 030601 (2009).
[30] A. Alvermann and H. Fehske, Phys. Rev. Lett. **102**, 150601 (2009).
[31] C. Zhang, E. Jeckelmann, and S. R. White, Phys. Rev. Lett. **80**, 2661 (1998).
[32] A. Weiße, H. Fehske, G. Wellein, and A. R. Bishop, Phys. Rev. B **62**, R747 (2000).
[33] Y. Nishiyama, Eur. Phys. J. B **12**, 547 (1999).
[34] A. K. Mitchell and R. Bulla, Phys. Rev. B **92**, 155101 (2015); A. K. Mitchell, P. G. Derry, and D. E. Logan, Phys. Rev. B **91**, 235127 (2015).
[35] A. Weichselbaum and J. von Delft, Phys. Rev. Lett. **99**, 076402 (2007).
[36] L. Borda, Phys. Rev. B **75**, 041307 (2007); B. Lechtenberg and F. B. Anders, Phys. Rev. B **90**, 045117 (2014).
[37] S. R. White, Phys. Rev. Lett. **69**, 2863 (1992); Phys. Rev. B **48**, 10345 (1993); U. Schollwöck, Rev. Mod. Phys. **77**, 259 (2005).
[38] U. Schollwöck, Ann. Phys. **326**, 96 (2011).
[39] C. Brockt, F. Dorfner, L. Vidmar, F. Heidrich-Meisner, and E. Jeckelmann, Phys. Rev. B **92**, 241106 (2015); F. A. Y. N. Schröder and A. W. Chin, Phys. Rev. B **93**, 075105 (2016); F. Dorfner and F. Heidrich-Meisner, Phys. Rev. A **93**, 063624 (2016).
[40] N.-O. Linden, Master's thesis, LMU Munich (2014).
[41] H.-J. Lee, R. Bulla, and M. Vojta, J. Phys. Cond. Matter **17**, 6935 (2005).

Supplementary material

The supplementary material presented below deals with four topics. Section S-1 offers a more detailed discussion of the construction of continued-fraction expansions and open Wilson chains. Section S-2 describes the numerical VMPS techniques used. Section S-3 is devoted to a detailed study of the dissipative harmonic oscillator, in order to benchmark our numerical methods against exact results. Section S-4 describes how the RG flow towards the Gaussian fixed point of the sub-ohmic spin-boson model for $0 < s \leqslant 0.5$ can be understood using scaling arguments.

S-1. DETAILED DISCUSSION OF CFE AND OWC CONSTRUCTION

Below we supply some technical details involved in the construction of (i) the continued-fraction expansion (CFE) and (ii) the open Wilson chain (OWC) presented in the main text. We begin in Subsection S-1 A with the case of a bath involving only a single flavor of excitations, as discussed in the main text. In Subsection S-1 B, we generalize the construction to a multi-flavor bath having a nondiagonal bath spectrum.

A. Single-flavor bath

(i) *Continued-fraction iteration step.*— We here give some details on the central step of the CFE, which takes a retarded correlator $\mathcal{G}_n$ as input and produces as output a self-energy, split into low- and high-energy contributions.

The input correlator $\mathcal{G}_n$, being retarded, has the spectral representation $\mathcal{G}_n(\omega) = \int d\bar{\omega}\, \frac{\mathcal{A}_n(\bar{\omega})}{\omega-\bar{\omega}+i0^+}$, with a spectral function, $\mathcal{A}_n(\omega) = -\frac{1}{\pi}\mathrm{Im}\,\mathcal{G}_n(\omega)$ that is normalized to unity, $\int d\omega \mathcal{A}_n(\omega) = 1$. If this correlator is represented in the form [Eq. (1)]

$$\mathcal{G}_n(\omega) = \frac{1}{\omega - \varepsilon_n - \Sigma_n(\omega)}\,, \tag{S1}$$

with $\Sigma_n(\omega)$ analytic in the upper half-plane as required for a retarded self-energy, then the constant in the denominator must be equal to the average energy of the spectral function $\mathcal{A}_n(\omega)$, $\varepsilon_n = \int d\omega\, \omega \mathcal{A}_n(\omega)$. In the main text this fact was used, but not explained. To understand its origin, invert Eq. (S1), multiply it by $\mathcal{G}_n(\omega)$, and integrate over frequency:

$$\begin{aligned}
\int d\omega\, \Sigma_n(\omega)\, \mathcal{G}_n(\omega) &= \int d\omega \left[(\omega-\varepsilon_n)\, \mathcal{G}_n(\omega) - 1\right] \\
&= \int d\omega \int d\bar{\omega} \left[\frac{\omega-\varepsilon_n}{\omega-\bar{\omega}+i0^+} - 1\right] \mathcal{A}_n(\bar{\omega}) \\
&= \int d\bar{\omega} \int d\omega \left[\frac{\bar{\omega}-\varepsilon_n}{\omega-\bar{\omega}+i0^+}\right] \mathcal{A}_n(\bar{\omega}) \\
&= -i\pi \int d\bar{\omega}\, (\bar{\omega}-\varepsilon_n)\, \mathcal{A}_n(\bar{\omega})\,.
\end{aligned} \tag{S2}$$

Since both $\mathcal{G}_n(\omega)$ and $\Sigma_n(\omega)$ are by assumption retarded functions and hence analytic in the upper half-plane, the left-hand side of the first line yields zero, as can be seen by closing the integration contour in the upper half-plane. The second line follows from the right-hand side of the first using the spectral representation of $\mathcal{G}_n$, and the fact that $\mathcal{A}_n$ is normalized to unity. Since the last line, being equal to the first, must equal zero too, it fixes ε_n to the value stated in above (again using the unit normalization of $\mathcal{A}_n$). Once ε_n has been fixed, the self-energy is fixed, too, by inverting Eq. (S1):

$$\Sigma_n(\omega) = \omega - \varepsilon_n - 1/\mathcal{G}_n(\omega). \tag{S3}$$

To summarize: The fact that the retarded correlator $\mathcal{G}_n(\omega)$ is analytic implies the same for its self-energy $\Sigma_n(\omega)$; this uniquely fixes ε_n and thus also $\Sigma_n(\omega)$ itself, which in turn can be viewed as a correlator with its own self-energy, etc. Thus, the analyticity of $\mathcal{G}_n(\omega)$ guarantees that it is always possible to iteratively construct a CFE for it. The new twist added to this well-known fact in the present work is to zoom in to small energies by splitting the self-energy into slow and fast parts and using only the former as input for the next iteration step.

To explicitly implement this splitting, given by Eq. (2),

$$\Sigma_n(\omega) = \Sigma_n^S(\omega) + \Sigma_n^F(\omega), \quad \Sigma_n^X(\omega) = |t_n^X|^2 \mathcal{G}_n^X(\omega), \tag{S4}$$

we proceed as follows. We split $\Gamma_n(\omega) = -\frac{1}{\pi}\mathrm{Im}\Sigma_n(\omega)$, which may be viewed as the bath spectrum of iteration n, into slow and fast parts, $\Gamma_n = \Gamma_n^S + \Gamma_n^F$, with

$$\Gamma_n^X(\omega) = w_n^X(\omega)\Gamma_n(\omega). \tag{S5}$$

Here the splitting functions $w_n^{S/F}(\omega)$ are defined on the support of Γ_n, take values in the interval $[0,1]$, satisfy $w_n^S(\omega) + w_n^F(\omega) = 1$, and have weight predominantly at low/high energies. Then we write the split bath spectra as $\Gamma_n^X(\omega) = |t_n^X|^2 \mathcal{A}_n^X(\omega)$, with "couplings" t_n^X chosen as

$$|t_n^X|^2 = \int d\omega\, \Gamma_n^X(\omega)\,, \tag{S6}$$

to ensure that the new spectral functions $\mathcal{A}_n^X(\omega)$ are normalized to unity. Using them to define new retarded correlators via $\mathcal{G}_n^X(\omega) = \int d\bar{\omega}\, \frac{\mathcal{A}_n^X(\bar{\omega})}{\omega-\bar{\omega}+i0^+}$, we obtain the desired slow/fast splitting of the self-energy stated above.

Next we describe the choice of splitting functions $w_n^X(\omega)$ used to obtain the numerical results of the main text. Let $I_n^S = [\omega_{Sn}^-, \omega_{Sn-}^+]$ denote the support of the slow spectral function $\mathcal{A}_n^S$. The bath spectrum for iteration n, $\Gamma_n(\omega) = -\frac{1}{\pi}\mathrm{Im}\,\Sigma_n(\omega)$, has support on the same interval, say I_n, as the correlator $\mathcal{G}_n = \mathcal{G}_{n-1}^S$, i.e. $I_n = I_{n-1}^S$. To implement the splitting $\Gamma_n = \Gamma_n^S + \Gamma_n^F$, we partition this interval into disjoint slow and fast subranges, $I_n = I_n^S \cup I_n^F$, with $|\omega_{Sn}^\pm| \leqslant |\omega_{Sn-1}^\pm|$, and use corresponding step-form splitting functions:

$$w_n^X(\omega) = \begin{cases} 1 \text{ for } \omega \in I_n^X, \\ \text{otherwise.} \end{cases} \tag{S7}$$

To ensure energy-scale separation, I_n^S should be chosen such that

$$\max\{|\varepsilon_n|, |t_n^S|\} \leqslant \max\{|\varepsilon_{n-1}|, |t_{n-1}^S|\}/\Lambda \tag{S8}$$

holds, with $\Lambda > 1$. If the bath spectrum $\Gamma^{\rm bath}(\omega)$ has a flat or power-law form, a natural choice is $\omega_{Sn}^{\pm} = \omega_{Sn-1}^{\pm}/\Lambda$. This is the choice used for the numerical work in the main text. However, if $\Gamma^{\rm bath}(\omega)$ has nontrivial structure, the choices for the subrange boundaries $\omega_{Sn}^{\pm}$ might have to be fine-tuned to ensure Eq. (S8) at each iteration. More generally, one might also explore using splitting functions $w_n^X(\omega)$ of smoother shape than those of Eq. (S7). The freedom of choice available for ensuring Eq. (S8) is one of the major strengths of the above strategy for generating a CFE.

(ii) *Construction of open Wilson chain.*— Here we provide some details on the construction of the OWC Hamiltonian of $\mathcal{H}_N^{\rm OWC}$ of Eq. (3). It describes a chain with $N+1$ sites, each coupled to a bath of its own, and site 0 coupled to the impurity (site -1) [Fig. 1(c)]. It is constructed such that the free ($t_{\rm imp} = 0$) correlator of site 0 is given by a depth-N CFE, $\mathcal{G}_0 = \mathcal{G}^{\rm bath}$.

We associate with each pair of correlators $\mathcal{G}_n^{S/F}$ from the CFE two mutually independent baths S_n and F_n. We regard $\mathcal{G}_n^X$ as the free retarded correlator of a normalized bath operator $b_{Xn}^\dagger$, whose dynamics is generated by a bath Hamiltonian $\mathcal{H}_n^X$, chosen such that $\mathcal{G}_n^X(\omega) = \langle\!\langle b_{Xn} || b_{Xn}^\dagger \rangle\!\rangle_\omega$ has the form found via the CFE.

We start our OWC construction by associating bath S_{-1} with the original bath [Fig. 1(b)], setting $\mathcal{H}_{-1}^S = \mathcal{H}^{\rm bath}$, $b_{S,-1}^\dagger = b^\dagger$ and $\mathcal{G}_{-1}^S = \mathcal{G}^{\rm bath}$, with impurity-bath coupling $t_{-1}^S = t_{\rm imp}$. We then proceed iteratively, starting with $n = 0$. The central CFE iteration step of writing $\mathcal{G}_{n-1}^S$ in the form of Eq. (1) corresponds, on the level of the Hamiltonian, to replacing the bath S_{n-1} by a new site n [Fig. 1(c)], with energy ε_n and normalized site operator $f_n^\dagger$, which is linearly coupled to two new baths, S_n and F_n, in such a way that its free ($t_{n-1}^S = 0$) site correlator $\mathcal{G}_n$ equals $\mathcal{G}_{n-1}^S$ [Eq. (1)]. To achieve this, we make the replacements $b_{Sn-1}^\dagger \to f_n^\dagger$ and

$$\mathcal{H}_{n-1}^S \to \varepsilon_n f_n^\dagger f_n + \sum_X (b_{Xn}^\dagger t_n^X f_n + \text{H.c.}) + \sum_X \mathcal{H}_n^X \ . \tag{S9}$$

Then $\mathcal{G}_n = \langle\!\langle f_n || f_n^\dagger \rangle\!\rangle_\omega$ indeed matches Eq. (1), since the self-energy generated for it by the new baths, $\Sigma_n(\omega) = \sum_X |t_n^X|^2 \mathcal{G}_n^X(\omega)$, agrees with Eq. (2). Since $\mathcal{G}_n = \mathcal{G}_{n-1}^S$, $f_n^\dagger$ and $b_{S,n-1}^\dagger$ have the same dynamics, i.e. the new site, bath S_n and bath F_n jointly have the same effect on site $n-1$ as the previous bath S_{n-1}. Now we iterate: we retain the fast bath F_n, but replace the slow bath S_n by a new site $n+1$ coupled to new slow and fast baths S_{n+1} and F_{n+1}, etc. After $N+1$ steps, the initial $\mathcal{H}$ has been replaced by the OWC Hamiltonian $\mathcal{H}_N^{\rm OWC}$ given in Eq. (3).

The above argument does not require the free Hamiltonians $\mathcal{H}_n^X$ and bath operators $b_{Xn}^\dagger$ to be constructed explicitly. For concreteness we specify them nevertheless:

$$\mathcal{H}_n^X = \sum_q \varepsilon_{qn}^X b_{Xqn}^\dagger b_{Xqn}, \quad b_{Xn}^\dagger = \sum_q b_{Xqn}^\dagger \lambda_{qn}^X \ . \tag{S10}$$

These involve a set of canonical annihilation and creation operators satisfying $[b_{Xqn}, b_{Xqn}^\dagger]_\pm = 1$ (+ for a fermionic anti-commutator, − for a bosonic commutator). The bath operators b_{Xn} are normalized to satisfy $[b_{Xn}, b_{Xn}^\dagger]_\pm = 1$. The free dynamics of $b_{Xn}^\dagger$, generated by $\mathcal{H}_n^X$, is characterized by the free retarded correlator and spectral function

$$\mathcal{G}_n^X(\omega) = \sum_q \frac{|\lambda_{qn}^X|^2}{\omega - \varepsilon_{qn}^X + i0^+}, \tag{S11a}$$

$$\mathcal{A}_n^X(\omega) = \sum_q |\lambda_{qn}^X|^2 \delta(\omega - \varepsilon_{qn}^X) \, . \tag{S11b}$$

The bath energies ε_{qn}^X and couplings λ_{qn}^X are assumed such that $\mathcal{G}_n^X(\omega)$ has the form obtained in the CFE.

B. Multi-flavor bath

Next we consider impurity models involving a multi-flavor bath with $m_{\rm f}$ flavors of excitations, labeled by an index $\nu = 1, \ldots, m_{\rm f}$. We assume that the impurity Hamiltonian $\mathcal{H}_{\rm imp}[b_\nu^\dagger]$, describing the impurity degrees of freedom and their coupling to the bath, depends on the bath only through $m_{\rm f}$ bath operators $b_\nu^\dagger$ and their conjugates b_ν, not necessarily normalized or orthogonal, with retarded correlator $\mathcal{G}_{\nu\nu'}^{\rm bath}(\omega) = \langle\!\langle b_\nu ; b_{\nu'}^\dagger \rangle\!\rangle_\omega$. We assume that the corresponding bath spectrum,

$$\Gamma_{\nu\nu'}^{\rm bath}(\omega) = -\big[\mathcal{G}_{\nu\nu'}^{\rm bath}(\omega) - \mathcal{G}_{\nu'\nu}^{\rm bath*}(\omega)\big]/(2\pi i) \, , \tag{S12}$$

is a specified, Hermitian, positive definite *matrix* function (i.e. for any given ω, the eigenvalues of the matrix are real and non-negative). Together with the form of $\mathcal{H}_{\rm imp}$, this matrix function fully determines the impurity dynamics. Models of this structure arise in studies of the Kondo compensation cloud [36], when considering multi-impurity situations [34], and in DMFT studies of multi-band lattice models, where $\Gamma_{\nu\nu'}^{\rm bath}(\omega)$ is constructed iteratively from the impurity spectral function $\mathcal{A}_{\nu\nu'}^{\rm imp}(\omega)$ computed at the previous DMFT iteration.

If $\Gamma_{\nu\nu'}^{\rm bath}(\omega)$ can be diagonalized using a frequency-independent unitary transformation, the eigenvalues, say $\Gamma_\nu(\omega)$, constitute $m_{\rm f}$ hybridization functions that can be discretized independently, using either standard Wilsonian discretization or our RWC discretization scheme. Here we are interested in the more general case that diagonalizing the bath spectrum requires a frequency-dependent unitary transformation, $\Gamma_{\nu\nu'}^{\rm bath}(\omega) = \sum_{\bar\nu} u_{\nu\bar\nu}^\dagger(\omega) \Gamma_{\bar\nu}(\omega) u_{\bar\nu\nu'}(\omega)$. This would be the case, for example, for DMFT studies of a fermionic lattice model with broken band degeneracy and spin-orbit coupling; the corresponding self-consistent impurity model is a

multi-band Anderson model involving nondiagonal level-bath couplings, leading to a nondiagonal impurity spectral function.

To treat this situation in Wilsonian fashion, one could write the bath spectrum as $\Gamma^{\rm bath}_{\nu\nu'}(\omega) = \int d\varepsilon_q \sum_{\bar\nu} v^\dagger_{q\nu\bar\nu}\,\delta(\omega-\varepsilon_q)\,v_{q\bar\nu\nu}$, with bath-lead matrix elements $v_{q\nu\nu'} = \sqrt{\Gamma_\nu(\varepsilon_q)}\,u_{\nu\nu'}(\varepsilon_q)$, and discretize the integral logarithmically (with the implicit assumption that $\Gamma_\nu(\omega)$ and $v_{q\nu\nu'}(\omega)$ change sufficiently slowly with ω that within a discretization interval they may be replaced by constants). We note, though, that the neglect of truncated bath modes is potentially more problematic for multi- than single-flavor models, since $\Gamma^{\rm bath}_{\nu\nu'}(\omega)$ will generically have matrix elements asymmetric in frequency.

Below we explain how multi-flavor models can alternatively be discretized using a generalization of our RWC construction. (We thank Andrew Mitchell for a stimulating discussion which led to this realization.) The overall strategy is completely analogous to the single-flavor case, but with a flavor index added to all creation and annihilation operators (e.g. $b^\dagger_{X n\nu}$), and two flavor indices to all matrix elements (e.g. $t^X_{n\nu\nu'}$) and correlators (e.g. $\mathcal{G}^X_{n\nu\nu'}$). We will mostly use a compact notation that suppresses these indices and indicates their implicit presence by an underscore, e.g. $\underline{b}^\dagger_{Xn}$, $\underline{t}^X_n$, $\underline{\mathcal{G}}^X_n$, $(\underline{b}^\dagger_{Xn}\underline{t}^X_n)_{\nu'} = b^\dagger_{Xn\nu}t^X_{n\nu\nu'}$, and $\underline{f}^\dagger_n\underline{\varepsilon}_n\underline{f}_n = \sum_{\nu\nu'} f^\dagger_{n\nu}\varepsilon_{n\nu\nu'}f_{n\nu'}$, etc.

Extracting normalized modes from bath spectrum.— The CFE to be constructed below involves a sequence of bath spectra with matrix structure, generically denoted by $\underline{\Gamma}(\omega)$. Each is a Hermitian, positive definite matrix function, $\underline{\Gamma}(\omega) = \underline{\Gamma}^\dagger(\omega)$. We would like to express such a function in terms of a Hermitian, positive definite matrix function $\underline{\mathcal{A}}(\omega)$ that is normalized as

$$\int d\omega\,\underline{\mathcal{A}}(\omega) = \underline{1}\,, \tag{S13}$$

because such an $\underline{\mathcal{A}}(\omega)$ can be viewed as the spectral function of a set of *orthonormal* bath modes. To this end, we note that the frequency integral $\underline{w} = \int d\omega\,\underline{\Gamma}(\omega)$ yields a Hermitian, positive definite matrix. (Reason: If two matrices are Hermitian and positive definite, the same is true for their sum, and similarly for an integral of such matrix functions.) The matrix $\underline{w}$ can thus be diagonalized in the form $\underline{w} = \underline{u}^\dagger\,\underline{d}\,\underline{u}$, with $\underline{u}$ unitary and $\underline{d}$ diagonal and positive. Then the matrix $\underline{t} = \underline{u}^\dagger\sqrt{\underline{d}}\,\underline{u}$ can be used to write the bath spectrum in the form

$$\underline{\Gamma}(\omega) = \underline{t}^\dagger\,\underline{\mathcal{A}}(\omega)\,\underline{t}\,, \tag{S14}$$

where both $\underline{t}$ and $\underline{\mathcal{A}}$ are Hermitian and positive definite, while $\underline{\mathcal{A}}$ by construction is normalized as in Eq. (S13). The first moment of $\mathcal{A}$ yields a Hermitian matrix, too: $\underline{\varepsilon} = \int d\omega\,\omega\,\underline{\mathcal{A}}(\omega)$. In the chain to be constructed below, $\underline{\varepsilon}$ plays the role of an onsite Hamiltonian and $\underline{t}$ that of a nearest-neighbor coupling. If desired, one may make another unitary transformation that diagonalizes either $\underline{\varepsilon}$ or $\underline{t}$, while leaving the normalization condition (S13) in tact.

Continued-fraction expansion.— As for the one-band case, we aim to iteratively represent $\underline{\mathcal{G}}^{\rm bath}(\omega)$ in terms of a sequence of continued-fraction expansions that zoom in on low energies. These involve a sequence of Hermitian, positive definite functions, $\underline{\mathcal{A}}^X_n(\omega) = \underline{\mathcal{A}}^{X\dagger}_n(\omega)$. Each is normalized to unity [Eq. (S13)] and can be viewed as the spectral function of a retarded correlator $\underline{\mathcal{G}}^X_n(\omega)$,

$$\underline{\mathcal{A}}^X_n(\omega) = -\big[\underline{\mathcal{G}}^X_n(\omega) - \underline{\mathcal{G}}^{X\dagger}_n(\omega)\big]/(2\pi i)\,, \tag{S15}$$

which in turn can be expressed as

$$\underline{\mathcal{G}}^X_n(\omega) = \int d\bar\omega \frac{\underline{\mathcal{A}}^X_n(\bar\omega)}{\omega-\bar\omega+i0^+}\,. \tag{S16}$$

The multi-band CFE construction follows the one-band case, except that all correlators carry underscores to indicate their matrix structure. First we initialize the CFE by expressing the bath spectrum in terms of a normalized spectral function, $\underline{\Gamma}^{\rm bath}(\omega) = \underline{t}^{S\dagger}_{\rm imp}\,\underline{\mathcal{A}}^S_{-1}(\omega)\,\underline{t}^S_{\rm imp}$ [cf. (S14)] and compute the corresponding retarded correlator $\underline{\mathcal{G}}^S_{-1}$ via Eq. (S16). Starting with iteration $n=0$, we then iteratively use $\underline{\mathcal{G}}^S_{n-1}$ as input to define a new retarded correlator $\underline{\mathcal{G}}_n$ and its retarded self-energy $\underline{\Sigma}_n$,

$$\underline{\mathcal{G}}_n(\omega) = \mathcal{G}^S_{n-1}(\omega) = 1/\left[\omega\underline{1} - \underline{\varepsilon}_n - \underline{\Sigma}_n(\omega)\right]\,, \tag{S17}$$

with $\underline{\varepsilon}_n = \int d\omega\,\omega\,\underline{\mathcal{A}}_n(\omega)$. Then we split this self-energy into low- and high-energy parts by writing it as

$$\underline{\Sigma}_n = \underline{\Sigma}^S_n + \underline{\Sigma}^F_n\,,\quad \underline{\Sigma}^X_n(\omega) = \underline{t}^{X\dagger}_n\underline{\mathcal{G}}^X_n(\omega)\underline{t}^X_n\,. \tag{S18}$$

To be concrete, we achieve this splitting by proceeding as follows. We split $\underline{\Gamma}_n(\omega) = -\big[\underline{\Sigma}_n(\omega) - \underline{\Sigma}^\dagger_n\big]/(2\pi i)$, the bath spectrum of iteration n, into slow and fast parts, $\underline{\Gamma}_n = \underline{\Gamma}^S_n + \underline{\Gamma}^F_n$, with

$$\Gamma^X_{n,\nu\nu'}(\omega) = w^X_{n,\nu\nu'}(\omega)\Gamma_{n,\nu\nu'}(\omega) \tag{S19}$$

(no index summation implied here), using symmetric, real matrix functions $\underline{w}^X_n(\omega)$. Their matrix elements $w^{S/F}_{n\nu\nu'}(\omega)$ are splitting functions that are defined on the support of $\underline{\Gamma}_n$, take values in $[0,1]$, have weight predominantly at low/high energies, and satisfy $w^S_{n\nu\nu'}(\omega) + w^F_{n\nu\nu'}(\omega) = 1$. (The simplest choice would be $\underline{w}^X_n(\omega) = w^X_n(\omega)\underline{1}$, using the same pair of weighting functions for all matrix elements; but situations may arise where the additional freedom of making different choices for different matrix elements is useful.) Since the splitting functions are symmetric and non-negative, the split spectra $\underline{\Gamma}^X_n$ are Hermitian and positive definite matrix functions, too. We can thus express them in terms of normalized spectral functions [Eq. (S14)]:

$$\underline{\Gamma}^X_n(\omega) = \underline{t}^{X\dagger}_n\underline{\mathcal{A}}^X_n(\omega)\underline{t}^X_n\,. \tag{S20}$$

Computing the corresponding retarded correlators $\underline{\mathcal{G}}^X_n$ [Eq. (S16)] we obtain the self-energy splitting stated in

Eq. (S18). To ensure energy-scale separation, the weighting functions $\underline{w}_n^X$ should be chosen such that

$$\max\{\|\underline{\varepsilon}_n\|, \|\underline{t}_n^S\|\} \leqslant \max\{\|\underline{\varepsilon}_{n-1}\|, \|\underline{t}_{n-1}^S\|\}/\Lambda \quad \text{(S21)}$$

holds, with $\Lambda > 1$, where $\|\ \|$ denotes some matrix norm.

Iterating this procedure yields a sequence of CFEs for $\underline{\mathcal{G}}^{\text{bath}}$, in the same fashion as for the one-band case.

Chain representation.— The CFE data $(\underline{\varepsilon}_n, \underline{t}_n^X, \underline{\mathcal{G}}_n^X)$ can now be used to represent the model in terms of a chain with $N+1$ sites, each coupled to a bath of its own. The chain is constructed such that the free ($\underline{t}_{-1}^S = 0$) correlator of the first site ($n = 0$) is given by a dept-N CFE. To this end, we associate each pair of correlators $\underline{\mathcal{G}}_n^{S/F}$ with two mutually independent baths S_n and F_n, and regard each $\underline{\mathcal{G}}_n^X$ as the free retarded correlator of a set of m_f normalized bath operators $\underline{b}_{Xn}^\dagger$, whose free dynamics is generated by a bath Hamiltonian $\mathcal{H}_n^X$, such that $\underline{\mathcal{G}}_n^X(\omega) = \langle\langle \underline{b}_{Xn} | \underline{b}_{Xn}^\dagger \rangle\rangle_\omega$. These free bath Hamiltonians and bath operators have the form

$$\mathcal{H}_n^X = \sum_q \underline{b}_{Xqn}^\dagger \underline{\varepsilon}_{qn}^X \underline{b}_{Xqn}\,, \quad \underline{b}_{Xn}^\dagger = \sum_q \underline{b}_{Xqn}^\dagger \underline{\lambda}_{qn}^X\,, \quad \text{(S22)}$$

where $\underline{\varepsilon}_{qn}^X$ and $\underline{\lambda}_{qn}^X$ are matrices w.r.t. to the flavor indices. $\underline{\varepsilon}_{qn}^X$ is diagonal and real, and $\underline{\lambda}_{qn}^X$ unitary, normalized such that $[\underline{b}_{Xn}, \underline{b}_{Xn}^\dagger]_\pm = \underline{1}$. The free bath correlators and spectral functions then have the explicit representations

$$\underline{\mathcal{G}}_n^X(\omega) = \sum_q \underline{\lambda}_{qn}^{X\dagger} \left[(\omega + i0^+)\underline{1} - \underline{\varepsilon}_{qn}^X\right]^{-1} \underline{\lambda}_{qn}^X\,, \quad \text{(S23a)}$$

$$\underline{\mathcal{A}}_n^X(\omega) = \sum_q \underline{\lambda}_{qn}^{X\dagger} \delta(\omega\underline{1} - \underline{\varepsilon}_{qn}^X) \underline{\lambda}_{qn}^X\,. \quad \text{(S23b)}$$

This representation for $\underline{\mathcal{A}}_n^X(\omega)$ shows explicitly that it is a Hermitian, positive definite matrix function.

The iterative OWC construction proceeds as for the single-flavor case, except that all operators, matrix elements and correlators now carry underscores to indicate implicit flavor indices. For example, the generalization of Eq. (S9) now involves the replacements $\underline{b}_{Sn-1}^\dagger \to \underline{f}_n^\dagger$ and

$$\mathcal{H}_{n-1}^S \to \underline{f}_n^\dagger \underline{\varepsilon}_n \underline{f}_n + \sum_X (\underline{b}_{Xn}^\dagger \underline{t}_n^X \underline{f}_n + \text{H.c.}) + \sum_X \mathcal{H}_n^X\,. \quad \text{(S24)}$$

The final OWC Hamiltonian has the same form as Eq. (3) of the main text, suitably decorated with underscores, and with $\mathcal{H}^{\text{imp}}[\underline{f}_0^\dagger \underline{t}_{\text{imp}}]$ as impurity Hamiltonian. Similarly, when moving on to a RWC, the energy shift equation (4) of the main text is decorated by underscores, i.e. we shift the onsite energy matrices $\underline{\varepsilon}_n$ by $\delta\underline{\varepsilon}_n^X$ shifts that should be chosen to optimize the truncated CFE representation of $\underline{\mathcal{G}}^{\text{bath}}$. We expect this step to be more important for multi- than single-flavor models, since $\underline{\Gamma}_n^X(\omega)$ will generically have matrix elements asymmetric in frequency. If one is interested mainly in correctly reproducing low-energy properties, one could choose $\delta\underline{\varepsilon}_n^X = \text{Re}\underline{\Sigma}_n^X(\omega = 0)$, as in the main text. Another option would be to view the $\delta\underline{\varepsilon}_n^X$ as fitting parameters, chosen to get the best possible agreement between the depth-n CFE for $\underline{\mathcal{G}}^{\text{bath}}(\omega)$ and its actual form.

S-2. NUMERICAL DETAILS

In this section, we elaborate on the details of the numerical methods employed in the main text. In Subsection S-2 A we briefly review NRG and its limitations in the context of bosonic impurity models. In Subsection S-2 B we discuss the VMPS techniques by which these limitations can be overcome. Finally, in Subsection S-2 C we present a generalized VMPS scheme that simultaneously targets multiple low-energy states on the Wilson chain, which enables us to generate the well-controlled energy-level flow diagrams for the sub-Ohmic spin-boson model (SBM) shown in Fig. 4 of the main text.

A. Bosonic NRG

The numerical renormalization group (NRG) is one of the most powerful tools to numerically evaluate the properties of quantum impurity models [1]. Wilson's formulation of "standard NRG" involves two steps. First, the model is represented in terms of a Wilson chain, i.e. a semi-infinite tight-binding chain whose hopping matrix elements t_n decrease exponentially with n, ensuring energy-scale separation along the chain. In the main text and Sec. S-1, we have described in detail how this is achieved for an RWC; for details on setting up a SWC we refer to Refs. [24] and [2]. Second, the chain is diagonalized iteratively one site at a time, discarding high-energy states at each step, to yield a set of so-called Wilson shells, where shell N contains the low-lying eigenstates of a finite chain whose last site is labelled N (a "length-N" chain). These shells can be used to calculate both thermodynamic and dynamical quantities; in particular, we employed the full-density-matrix NRG scheme (fdm-NRG) to evaluate thermal averages of observables in this work [35].

Whereas NRG has been highly successful in the context of fermionic impurity models, its application to bosonic baths has been impeded by two numerical issues, (i) the mass-flow error and (ii) the local Hilbert space truncation. We elaborated on (i) in detail in the main text. We add that NRG cannot be completely cured from the mass flow using the C2-RWC construction, as discussed in more detail in Sec. S-3 below. This is related to the iterative nature of the NRG diagonalization procedure, which does not allow to incorporate any feedback of the slow-mode correction to earlier iterations, in contrast to the variational setup presented in Sec. S-2 B below. Problem (ii) is related to the fact that only a limited number of bosons can be included in an NRG calculation. NRG requires an *a priori* truncation of the infinite-dimensional

local bosonic Hilbert space on each site n to a numerically feasible number of d_n bosonic states. For example, for the spin-boson model NRG is therefore not able to accurately deal with the fact that the oscillator displacement occurring in the localized phase grows exponentially along the Wilson chain, which implies that the number of bosons in the standard oscillator representation must increase exponentially, too [16].

In the context of the sub-Ohmic SBM, it has been thoroughly illustrated how the limitations of bosonic NRG can tamper with physical properties. Here, the interplay of these two numerical issues affected a number of critical exponents, causing them to follow hyperscaling instead of mean-field results for $0 < s < 0.5$ [15]. The internal consistency of these NRG results (which were later shown to be incorrect) was so striking that it initially lead to the controversial conclusion, that the quantum-to-classical correspondence breaks down in case of the sub-Ohmic SBM. This subtle "conspiracy of errors" [27] implies that NRG is not fully equipped to deal with bosonic baths, since parts of the phase diagram and, in particular, the impurity quantum phase transition, may not be reliably accessible for the method.

B. VMPS with optimal boson basis

The intrinsic flaws of bosonic NRG can be completely dealt with by employing the strategy of the density matrix renormalization group (DMRG) to treat RWC Hamiltonians [4, 37]. To this end, we use the matrix-product-state (MPS) formulation of DMRG [38], which we refer to as variational matrix-product-state approach (VMPS) in the following [3, 4]. This method can overcome the issue of Hilbert space truncation by using a flexible, shifted optimized boson basis (OBB) [31], as shown in [6, 39]. Moreover, the mass-flow problem can be successfully cured by performing the variational procedure on C2-RWCs, as demonstrated in the main text. We briefly elaborate on the main aspects of the VMPS approach and refer to [6] for technical details.

The goal of the VMPS approach is to efficiently represent the ground state of a Wilson chain with N bath sites in the formalism of matrix-product states [38]. A generic MPS of a bosonic impurity model has the form

$$|\psi\rangle = \sum_{\sigma,\mathbf{m}} A^{[\sigma]} A^{[m_0]} A^{[m_1]} \dots A^{[m_N]} |\sigma\rangle|\mathbf{m}\rangle\,, \qquad \text{(S25)}$$

where $|\sigma\rangle$ represents the local space of the impurity (e.g., a spin-$\frac{1}{2}$ degree of freedom) and $\mathbf{m} = |m_0\rangle ... |m_N\rangle$ describes the local boson number eigenstates in a truncated Fock basis, i.e., $f_n^\dagger f_n |\mathbf{m}\rangle = m_n |\mathbf{m}\rangle$ with $m_n = 0, 1, ..., d_n - 1$. Starting with a random MPS, the ground state is approximated by iteratively varying the tensors $A^{[\dots]}$ to minimize the energy of the Wilson chain Hamiltonian, sweeping back and forth through the chain until a global energy minimum is reached with sufficient convergence.

One key advantage of VMPS over NRG is the ability to flexibly adapt the local bosonic state basis on each site of the Wilson chain during the optimization process. This concept of an adaptive boson basis enables us, for example, to determine the ground state also in the localized phase of the SBM faithfully, which is not possible in NRG calculations. Our OBB implementation includes two features: First, we introduce an additional basis transformation V with $V^\dagger V = \mathbb{1}$, which maps the local harmonic oscillator basis $|m_n\rangle$ onto a smaller effective basis $|\tilde{m}_n\rangle$ on each site n,

$$|\tilde{n}_n\rangle = \sum_{m_n=0}^{d_n-1} V_{\tilde{m}_n, m_n} |m_n\rangle \quad (\tilde{m}_n = 0, \dots, \tilde{d}_n - 1)\,. \qquad \text{(S26)}$$

V can be naturally embedded in the MPS structure and is optimized in an additional local update to determine the best set of local basis states $|\tilde{m}_n\rangle$ for the subsequent update steps [6].

Second, we explicitly incorporate any oscillator displacements occurring in strong-coupling phases when constructing the local boson basis sets. To this end, we shift the oscillator coordinate $\hat{x}_n = \frac{1}{\sqrt{2}}(f_n + f_n^\dagger)$ on each site n by its equilibrium value $\langle \hat{x}_n \rangle$ [30] employing an unitary transformation to the Hamiltonian of the system [6]. $\langle \hat{x}_n \rangle$ can be determined self-consistently in a variational setting. Using such a setup, the OBB is able to capture quantum fluctuations around the shifted coordinate $\hat{x}'_n = \hat{x}'_n - \langle \hat{x}_n \rangle$.

In practice, the shifted OBB not only allows a significant increase of the size of the local basis sets from $d_n \approx \mathcal{O}(10^2)$ to $d_n \lesssim \mathcal{O}(10^4)$ by means of the basis transformation V. In addition, the shifted oscillator basis enables us to account for the exponentially growing oscillator displacements in a numerically quasi-exact way, which would require a local dimension of up to $d_n^{\text{eff}} \approx (10^{10})$ in a nonshifted basis [6].

An additional advantage of the variational optimization over NRG is the fact that the former typically involves multiple sweeps along the chain, so that information from different parts of the Wilson chain (i.e., from different energy scales) is incorporated during the optimization process. This feedback mechanism is not needed for chains that have energy-scale separation. However, the latter is violated at the last site of a C2-RWC, where the slow-mode energy shift is large enough to affect the nature of the MPS not only on the last site but also on several preceding sites. In contrast to NRG, the VMPS approach is capable of feeding back this slow-mode information from low-energy scales to higher ones during the optimization sweeps, which is key to successfully avoid any mass-flow effects.

Even though the VMPS scheme described above only targets the ground state, it can be used to mimic finite-temperature averages on the Wilson chain, such as the thermal average $\langle a + a^\dagger \rangle_T$ or $\langle \hat{\sigma}_z \rangle_T$ needed to compute the local susceptibility $\chi(T)$ for the DHO or SBM, respectively. To this end, we compute the ground-state expecta-

tion value $\langle \mathrm{G}|a+a^\dagger|\mathrm{G}\rangle_{N_T}$ or $\langle \mathrm{G}|\hat{\sigma}_z|\mathrm{G}\rangle_{N_T}$ for a length-N_T C2-RWC, where N_T is chosen such that the chain's lowest energy scale matches the temperature, $T \sim \Lambda^{-N_T}$. This works because, for a length-N_T chain, the response of the ground state is calculated for a discrete spectrum whose low-energy excitations have characteristic spacing T. This is the strategy that was used for the VMPS calculations of $\chi(T)$ reported in the main text. A more detailed description of this strategy is given in Sec. S-3 below, devoted to a detailed study of the dissipative harmonic oscillator (DHO). There we compare several different strategies for computing thermal averages and benchmark their results against the exact solution for $\chi(T)$.

An important prerequisite for studying critical properties is a highly accurate determination of the critical coupling α_c. Numerically, it can be found in several ways. First, by determining the α-value at which the susceptibility $\chi(T=0)$ diverges; this was our method of choice in the context of the DHO. Second, by monitoring how the NRG or VMPS energy flow diagrams evolve with α. For the SBM there exist a third option, namely monitoring the behavior of the average boson occupation per site, $\langle m_n\rangle$: at the phase boundary it stays almost constant throughout the chain, but in the delocalized (localized) phase it decreases (increases) towards the end of the Wilson chain. We used the third scheme for the SBM, since it can be automated very easily. C2-chains sometimes required additional fine-tuning, since the slow-mode shift always increases the occupation numbers at the end of the chain.

We end this section with some technical notes. All VMPS ground-state calculations in this work for both DHO and SBM were performed using a 1-site update with fixed bond dimension $D = 60$, $d_n = 100$, and $\tilde{d}_n = 16$. Convergence was assumed if the change in the chain's ground-state energy dropped below the threshold $|\delta E_\mathrm{G}| < 10^{-15}$, which for our longest chains corresponded to $\simeq 0.5$ of the hopping matrix element t_N to the last site. This typically took 10 to 50 sweeps. For the determination of the temperature-dependent susceptibility $\chi(T)$, we performed separate VMPS calculations for each value of T and used a five-point stencil to evaluate the numerical derivative with respect to ϵ. The convergence of the results with respect to all important numerical parameters was checked thoroughly.

C. Multilevel VMPS

The study of energy-level flow during the renormalization procedure is an important part of the NRG toolbox to characterize the fixed-point properties of an impurity model. However, in the presence of the mass-flow error, prominent for a bosonic bath with asymmetric bath spectrum, NRG does not correctly capture the physics of the critical fixed point and the resulting RG flow can no longer be considered reliable. On the other hand, we have already demonstrated that VMPS techniques are able to appropriately deal with mass flow; below we show that they can also be employed to properly access the energy-level flow at quantum critical points.

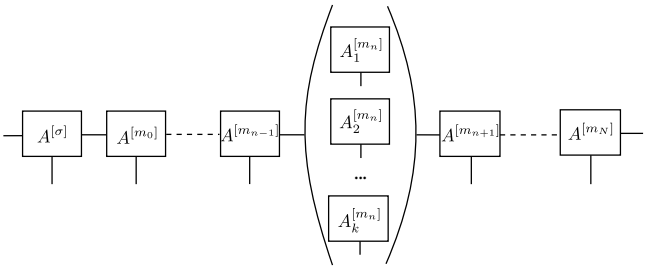

Figure S1. Illustration of mVMPS setup for variationally calculating the m lowest-energy excitation on a Wilson chain.

In its standard formulation, described above, VMPS only targets the ground state and does not have sufficient information about low-lying excited states on the Wilson chain to accurately describe the energy-level flow. In order to go beyond ground-state physics and properly capture the critical energy-level RG flow of multiple low-lying levels, we have implemented a multi-level VMPS (mVMPS) optimization scheme, in the spirit of Ref. [5], that simultaneously targets the lowest k energy eigenstates $|\psi_j\rangle$. A detailed description of our procedure may be found in Sec. 2.3.6 of [40]. Here we just outline the main idea.

Assuming canonical form of the MPS with the center shifted to site n, we define an array $\mathbf{A}^{[m_n]}$ consisting of k tensors $\{A_1^{[m_n]}, A_2^{[m_n]}, \ldots, A_k^{[m_n]}\}$ (illustrated in Fig. S1). For each tensor $A_j^{[m_n]}$, with $j = 1, ..., k$, the state

$$|\psi_j\rangle = \sum_{\sigma,\mathbf{m}} A^{[\sigma]}A^{[m_0]}...A^{[m_{n-1}]}A_j^{[m_n]}A^{[m_{n+1}]}...A^{[m_N]}|\sigma\rangle|\mathbf{m}\rangle, \tag{S27}$$

describes one of the k lowest-energy eigenstate of the specified Wilson chain Hamiltonian; the state corresponding to $j = 1$ targets the ground state. The optimization procedure then works as follows: we generate a local Krylov space on site n by subsequent application of the Hamiltonian on each of the k orthonormal states associated with the array $\mathbf{A}^{[m_n]}$. The resulting Hamiltonian $\hat{H}_n$ has a block structure in the Krylov space, with nonzero elements in form of $k \times k$ blocks along the diagonal and the first off-diagonal. Next, we diagonalize the Hamiltonian in the Krylov subspace and construct from its eigenvectors an updated version of the array $\mathbf{A}^{[m_n]}$, each element being orthonormal to the others by construction. To move the orthonormal center of the MPS to the next site $(n+1)$, we form the reduced density matrix $\rho_{n,n+1}^{\mathrm{red,j}}$ of each component j by tracing out the rest of the chain and sum them up to form $\rho_{n,n+1}^{\mathrm{red}}$. Similar to the original DMRG formulation, we then diagonalize $\rho_{n,n+1}^{\mathrm{red}}$, keep only the D largest eigenvalues and use the resulting

isometry to move the orthonormal center to site $n+1$. We repeat the optimization procedure, sweeping multiple times through the entire chain. Convergence was assumed when the change in each energy level E_j dropped below the threshold $|\delta E_j| < 10^{-11}$, which for our longest multi-level chains corresponded to $\simeq 10^{-3}$ of the hopping matrix element t_N to the last site. In all mVMPS calculations we used bond dimensions of $D = 100$, $d_n = 40$.

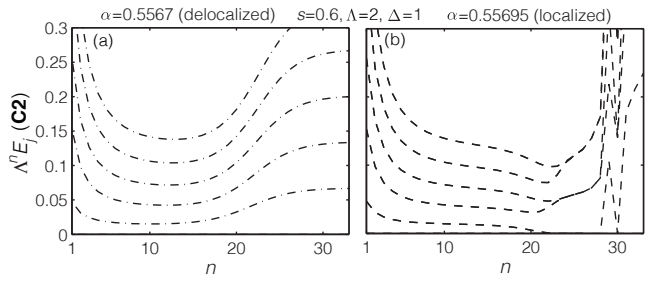

Figure S2. Energy-flow diagrams obtained with mVMPS for the SBM on a C2-RWC. (a) Flow to the delocalized fixed point, characterized by a unique ground state. (b) Flow to the localized fixed point, featuring a doubly degenerated ground-state level. Note that the flow gets distorted deep in the localized regime. This is a signature of the exponentially growing oscillator shifts which cannot be properly dealt with in the mVMPS setup.

To account for the mass flow in the energy-level flow of a length-N RWC system, we conduct a *separate* mVMPS calculation for *every* chain length $N' < N$. This ensures that the k excited states properly take into account the fast- and slow-mode correction at a particular energy scale, which is crucial for correctly describing the critical energy flow at a Gaussian fixed-point. Combining the results for various lengths and rescaling each set of energies appropriately by a factor $\Lambda^{N'}$, we obtain the energy-flow diagrams in a variational setup.

In addition to the critical fixed-point flows shown in Fig. 3 of the main text, we here present the energy-flow to the stable fixed points in Fig. S2. Panel (a) displays the energy flow to the delocalized fixed point ($\alpha < \alpha_c$), which features a nondegenerate ground state. In contrast, the fixed point flow to the localized fixed point ($\alpha > \alpha_c$) in panel (b) clearly shows a doubly degenerated ground state before getting numerically distorted by the exponentially growing oscillator displacements.

The main goal of our mVMPS calculations was to study the *critical* energy-level flow for the SBM. Since at the critical point the truncation of the bosonic Hilbert space is not problematic, it was not necessary to incorporate the OBB scheme in our mVMPS setup. Doing so would become essential, however, when studying the effects of a local bias, $\epsilon \neq 0$, since then $\langle\hat{\sigma}_z\rangle \neq 0$. In particular, this would be needed if one wishes to compute the static susceptibility $\chi(T)$ using not just the VMPS ground-state expectation value for a length-N_T RWC (as described above), but a thermal average over a shell of low-lying VMPS eigenstates (as done in NRG). We have refrained from attempting such combined mVMPS+OBB computations of $\chi(T)$, since they are numerically expensive, and the ground-state-based scheme worked very well.

S-3. DISSIPATIVE HARMONIC OSCILLATOR

In this section, we perform a systematic study of the properties of RWCs in the context of the exactly solvable DHO, which was briefly introduced in the main text. We compare the RWC and SWC setups in detail with respect to the following issues: iteration details, static susceptibility, and critical coupling α_c.

A. Iteration details

We introduced two types of RWCs in the main text: C1 chains, which include only the fast shifts ($\delta\varepsilon_N^S = 0$), and C2 chains, which contain both slow- and fast-mode shift in Eq. (4). For completeness, we also discuss a third type of RWC to be called C0 chains, which by definition include no energy shifts, i.e. $\delta\epsilon_n^{S/F} = 0$ in Eq. (4).

We have explored two versions of the RWC iteration scheme, that differ only in the choice of the frequencies ω_{Sn}^+ that define the intervals $I_n^S = [0, \omega_{Sn}^+]$. For version 1, we chose ω_{Sn}^+ in such a manner that the resulting hopping matrix elements t_n^S of the OWC agree with those used by Bulla, Tong and Vojta (BTV), [24] to be called $t_n^{\rm BTV}$ [Eq. (13) of Ref. 24], with relative error below 10^{-3}. (The error could be further reduced, if desired, by using a finer frequency grid for representing $\Gamma_n(\omega)$, and more accurately fine-tuning the numerical integration routine used to evaluate the integral that yields t_n^S.) For version 2, we used a plain exponential discretization, $\omega_{Sn}^+ = \omega_{Bn}^+/\Lambda$.

A comparison of the resulting t_n^S, the bare onsite energies ε_n and the shifts $\delta\varepsilon_n^{F/S}$, is shown in Fig. S3. It has two take-home messages: First, all these quantities scale the same way with n and are comparable in magnitude [Figs. S3(a,b)]. In particular, the fast and slow shifts $\delta\varepsilon_n^{F/S}$ are comparable to the bare OWC energies ε_n. Second [Figs. S3(d)], our RWT energies, both $\varepsilon_n + \delta\varepsilon_n^F$ and $\varepsilon_n + \delta\varepsilon_n^F + \delta\varepsilon_n^S$, are in general different from the SWC onsite energies $\varepsilon_n^{\rm BTV}$ obtained by BTV using standard Wilsonian discretization and tridiagonalization, the relative difference being $\mathcal{O}(1)$. For version 1, however, we note that the relative difference between $\varepsilon_n + \delta\varepsilon_n^F$ and $\varepsilon_n^{\rm BTV}$ becomes negligible for after a few iterations, but for early ones the difference remains.

Note that we also explored a third discretization scheme similar to version 1, with the difference that we fixed the truncation energies ω_{Sn}^+ such that the resulting hoppings agree with those resulting from the improved logarithmic discretization recently proposed by Zitko and Pruschke (ZP) [26]. This leads to results qualitatively

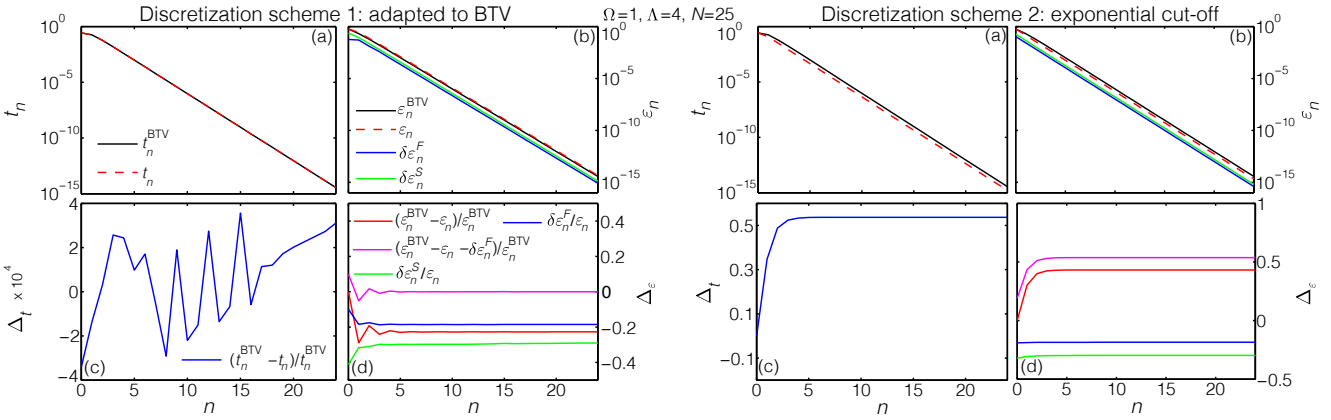

Figure S3. Iteration details: chain parameters. (a-d) Comparison of the Wilson chain parameters t_n and ε_n for $\alpha = 0.199$, obtained using the standard discretization scheme of BTV [24] for $\Lambda = 4$, or using two versions of the RWC-approach described above: for version 1 (left two columns), $\omega_{S,n}$ was fine-tuned to ensure that $t_n = t_n^{\rm BTV}$; for version 2 (right two columns), we simply chose $\omega^+_{Sn} = \omega^+_{Sn-1}/\Lambda$. (a) $t_n^{\rm BTV}$ used by BTV (black) and our t_n^S (red dashed). (b) The onsite energies $\varepsilon_n^{\rm BTV}$ (black), our C0 onsite energies ε_n (red dashed), and the shifts $|\delta\varepsilon_n^F|$ (blue) and $|\delta\varepsilon_n^S|$ (green). Evidently, they all scale the same way with n. (c) Relative difference $\Delta_t = (t_n^{\rm BTV} - t_n^S)/t_n^{\rm BTV}$ in hopping elements. The noisy structure seen for version 1 (left, note the amplification factor of 10^4) reflects the ω-discretization grid used to represent the bath correlators $\mathcal{G}_n^X(\omega)$ during the OWC construction. (d) Relative differences Δ_ε of various onsite energies: $\Delta_\varepsilon^{\rm C0} = (\varepsilon_n^{\rm BTV} - \varepsilon_n)/\varepsilon_n^{\rm BTV}$ (red); $\Delta_\varepsilon^{\rm C1} = (\varepsilon_n^{\rm BTV} - \varepsilon_n - \delta\varepsilon_n^F)/\varepsilon_n^{\rm BTV}$ (purple); $\Delta_\varepsilon^F = \delta\varepsilon_n^F/\varepsilon_n$ (blue); and $\Delta_\varepsilon^S = \delta\varepsilon_n^S/\varepsilon_n$ (green). For version 1 (left), the relative difference between BTV and C0 energies (no shifts) is quite significant throughout ($\Delta_\varepsilon^{\rm C0} \simeq 0.2$). The relative difference between BTV and C1 energies (only fast shifts) is significant for early iterations, but becomes small ($\Delta_\varepsilon^{\rm C1} \lesssim 10^{-3}$) once the iteration scheme reaches self-similarity. For version 2 (right), both $\Delta_\varepsilon^{\rm C0}$ and $\Delta_\varepsilon^{\rm C1}$ differ significantly from 0. Both the fast and last slow mode shifts are comparable in magnitude to the bare OWC energies, $\mathcal{O}(\Delta_\varepsilon^{F/S}) = 1$.

similar to those of version 1, therefore we refrained from including them in the discussion above.

The results in the main text were obtained using version 2. This discretization scheme is particularly appealing due to its accuracy and simplicity. It is more accurate than standard Wilsonian discretization, since by construction it reproduces the hybridization function correctly. The discretization scheme of ZP was devised to achieve this, too, but our scheme turns out to be more accurate, due to its inclusion of TBMs (compare green and red symbols in Fig. S5 below). Our discretization scheme is also simpler to implement than that of ZP, since their chain parameters are found by solving a differential equation, whereas our chain parameters (fixed fully by the energies $\tilde{\varepsilon}_n$ and couplings t_n^S) are found purely by numerical integrations. The accuracy of the latter can be easily controlled by distributing the grid points logarithmically and, in particular, increasing the resolution around the cut-off frequencies ω_{Sn^+}. Note that our discretization scheme offers great flexibility, as one can easily relax the logarithmic discretization in favour of a linear or mixed one (log-linear or linear-log) if high- or low-energy properties need to be taken into account more carefully [4]. (The resulting chain would then have to be treated purely with VMPS methods.)

In addition, we have also examined the retarded self-energies Σ_n^S generated in different iterations n and checked to what extent our chain parameters reproduce the original bath correlator $\mathcal{G}^{\rm bath}$ [Fig. S4]. (In this context, the two discretization schemes yield qualitatively similar results, so that Fig. S4 only displays version 2.) The main conclusion drawn from the real and imaginary part of Σ_n^S [Figs. S4(a,b)] for the power-law coupling spectrum $\Gamma^{\rm bath}$ considered here is that the iteration scheme has a self-similar structure, in that the shape of ${\rm Re}[\Sigma_n^S(\omega)]$ and ${\rm Im}[\Sigma_n^S(\omega)]$ vs. ω/ω_{Sn} does not change with n. Moreover, the continued fraction expansion of $\mathcal{G}^{\rm bath}$ [Figs. S4(c-f)] fully reproduces the original function (black) if both the fast- and last mode contributions $\Sigma_n^{F/S}(\omega)$ are included (dashed red), but if these are neglected (dashed green, cyan, blue), the low-frequency behavior changes significantly.

B. Various averaging schemes

For the VMPS calculations of $\chi(T)$ reported in the main text, we mimicked thermal averages by ground-state expectation values of C2-RWCs of length N_T. However, we have also explored several other averaging schemes. For the sake of completeness, we briefly describe them here, and in the next section compare their results for the susceptibility of the DHO.

For a RWC of specified length N, we have explored the following ways of calculating ground-state expectation values or thermal averages, distinguished by combinations of the following labels: W stands for *Wilsonian*

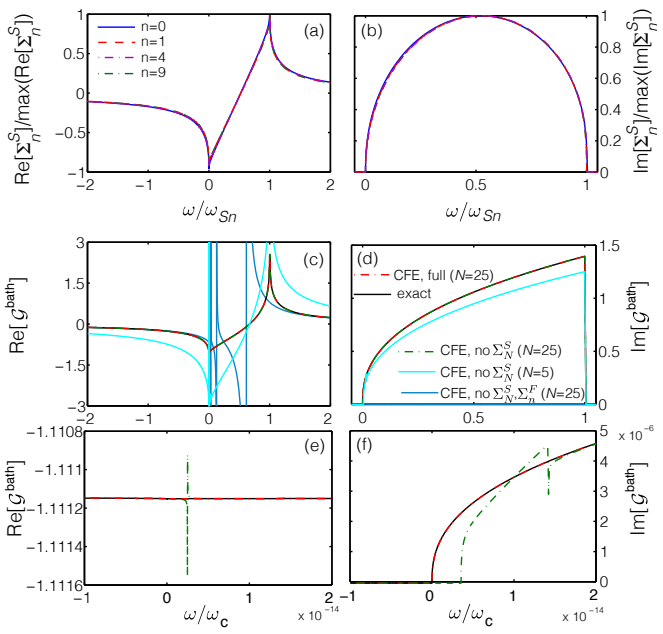

Figure S4. Iteration details: self-energies. (a) $\mathrm{Re}[\Sigma_n^S(\omega)]$ and (b) $\mathrm{Im}[\Sigma_n^S(\omega)]$, plotted vs. ω/ω_{Sn}^+ for $n = 0, 1, 4, 9$ (different colors), showing that the spectral functions and self-energies have a self-similar structure. (c-f) Various CFE representations of $\mathcal{G}^{\mathrm{bath}} = \mathcal{G}_0$. (c) $\mathrm{Re}[\mathcal{G}^{\mathrm{bath}}(\omega)]$ and (d) $\mathrm{Im}[\mathcal{G}^{\mathrm{bath}}(\omega)]$ vs. ω/ω_c, calculated directly from $\Gamma^{\mathrm{bath}}(\omega)$ (solid black), or from a CFE while including both $\Sigma_n^F(\omega)$ and $\Sigma_N^S(\omega)$ with $N=25$ (dashed red), only $\Sigma_n^F(\omega)$ with $N=5$ (cyan) or $N=25$ (dashed green), or neither of the two with $N=25$ (blue). In the latter case, the absence of any imaginary parts in the CFE causes $\mathrm{Im}[\mathcal{G}^{\mathrm{bath}}(\omega)]$ to vanish and $\mathrm{Re}[\mathcal{G}^{\mathrm{bath}}(\omega)]$ to have divergences. Behavior of (e) $\mathrm{Re}[\mathcal{G}^{\mathrm{bath}}(\omega)]$ and (f) $\mathrm{Im}[\mathcal{G}^{\mathrm{bath}}(\omega)]$ for $\omega \to 0$ with the same color code as in (c,d). The missing slow-mode term in the CFE using only $\Sigma_n^F(\omega)$ (green) causes discrepancies for both the imaginary and the real part only in the vicinity of $\omega = 0$ illustrating that the effect of slow-mode shifts becomes noticeable only at the lowest energy scale of a Wilson chain, associated with its last site.

NRG with energy-based truncation; V for *variational* MPS; G for a ground-state expectation value; and T for a thermal average. For Wilsonian NRG calculations, we denote the eigenstates and -energies of Wilson shell n by $|s\rangle_n^{\mathrm{W}}$ and E_{sn}^{W}, and by $|\mathrm{G}\rangle_n^{\mathrm{W}}$ and $E_{\mathrm{G}n}^{\mathrm{W}}$ for that shell's ground state. For VMPS calculations, we variationally minimize the ground-state expectation value of a length-N RWC in the space of all MPS having specified matrix dimensions. Call the resulting ground state $|\mathrm{G}\rangle_N^{\mathrm{V}}$, with energy $E_{\mathrm{G}N}^{\mathrm{V}}$.

We write $\langle\hat{O}\rangle_N^{\mathrm{G}Z} = {}_N^Z\langle\mathrm{G}|\hat{O}|\mathrm{G}\rangle_N^Z$ for a ground-state expectation value of type $Z = \mathrm{W}$ or V. We write N_T for the length of a RWC whose smallest excitation energies are comparable to the temperature,

$$\max\{|\tilde{\varepsilon}_{N_T}|, |t_{N_T}^S|\} \simeq T, \tag{S28}$$

and $\langle\hat{O}\rangle_{N_T}^{\mathrm{TW}}$ for a thermal average over all Wilson shell states $|s\rangle_{N_T}^{\mathrm{W}}$. We will call this TW-averaging. Thermal averages can also be mimicked using a single state associated with a length-N_T chain, e.g. $\langle\hat{O}\rangle_{N_T}^{\mathrm{G}Z} = {}_{N_T}^Z\langle\mathrm{G}|\hat{O}|\mathrm{G}\rangle_{N_T}^Z$ (GW- or GV-averaging), because, by the choice of N_T, the characteristic energy spacing for low-energy excitations above such a state is of order T. GW-, TW- and GV-averaging require calculating a separate length-N_T chain for every temperature.

C. Susceptibility

In this section, we compare the various types of RWCs discussed above (C0,C1,C2) and the various averaging schemes by using them to calculate the static susceptibility of the DHO. It is defined by

$$\chi(T) = \lim_{\epsilon\to 0} \frac{d\langle a + a^\dagger\rangle_T}{d\epsilon} , \tag{S29}$$

where $\langle\ldots\rangle_T$ denotes a thermal expectation value. Its form is easily found analytically [17],

$$\chi_{\mathrm{exact}}(T) = \frac{1}{\Omega + \mathrm{Re}(\mathcal{G}^{\mathrm{bath}}(\omega = 0))} , \tag{S30}$$

which, importantly, is independent of temperature.

Alternatively, the static susceptibility can also be calculated via the dynamical correlation function

$$C(\omega) = \frac{1}{2\pi}\int_{-\infty}^{\infty} e^{i\omega t} C(t)\mathrm{d}t , \tag{S31}$$

where $C(t) = \frac{1}{2}\langle[(a + a^\dagger)(t), (a + a^\dagger)]\rangle_T$. The integral

$$\chi_{\mathrm{dyn}}(T) = 4\int_0^{\infty} \frac{C(\omega)}{\omega}\mathrm{d}\omega \tag{S32}$$

can analytically be shown to equal the static susceptibility, $\chi(T) = \chi_{\mathrm{dyn}}(T)$, yielding an important consistency check for numerical calculations. Our Wilsonian NRG calculations passed this check for all three types of RWC introduced above (C0, C1, C2), where $\chi(T)$ was calculated by evaluating $\langle\ldots\rangle_T$ in Eq. (S29) using a Wilson-shell thermal average $\langle\ldots\rangle_{N_T}^{\mathrm{TW}}$, and $\chi_{\mathrm{dyn}}(T)$ was calculated using fdm-NRG [35]. This illustrates the internal consistency of Wilsonian NRG for a given RWC. However, none of these calculations reproduce the exact result (S30). In contrast, the latter *is* reproduced correctly when calculating χ using VMPS on chain type C2, as we now discuss in detail.

Fig. S5 shows $\chi(T)$ for three types of RWC, C0 (blue), C1 (green), and C2 (red), calculated in four different ways, involving either a CFE (solid lines), or a thermal average over Wilson shell N_T (TW, triangles), or two types of expectation values w.r.t. states associated with site N_T (GW, GV), as detailed in the figure caption. We observe the following salient features.

First, all four methods yield mutually consistent results both for C0 and for C1, but not for C2 (all orange

data lie on a line, as do all blue data, but not all red data). Thus the methods differ mainly in their treatment of slow last modes, which are absent in C0 and C1, but present in C2.

Second, for C0 (orange), which has the structure of a *standard* Wilson chain without any TBM information included, $\chi_{\rm C0}(T)$ differs from the exact result, $\chi_{\rm exact}$ (dashed black line) in two important ways: instead of being T-independent, $\chi_{\rm C0}(T)$ increases with decreasing T, eventually saturating toward a constant value, $\chi_{\rm C0}(0)$; and this constant value disagrees from $\chi_{\rm exact}$. The reason for these failings was identified clearly by VBGA [17]: the neglect of TBMs causes $\mathrm{Re}[\mathcal{G}^{\rm bath}(0)]$ to be represented incorrectly [as is also clearly visible in Fig. S4(c)]. VBGA called the missing contribution to $\mathrm{Re}[\mathcal{G}^{\rm bath}(0)]$ a "mass-flow" error (since near a quantum phase transition, it implies an artificial scale-dependent shift of the order-parameter mass).

Third, for C1 (blue), which includes fast but not last slow modes, the T-dependence of $\chi_{\rm C1}(T)$ persists, but its asymptotic low-temperature value agrees with the exact one, $\chi_{\rm C1}(0) = \chi_{\rm exact}$. Thus, including fast modes is essential to get the asymptotic value right. Indeed, if they are omitted but the slow mode correction included, one obtains curves (not shown) whose $T \to 0$ limits corresponds to those of C0 curves rather than the exact result.

Fourth, for C2 (red), which includes fast and last slow modes, two methods fully reproduce the *T-independent* result $\chi_{\rm C2}(T) = \chi_{\rm exact}$: CFE and GV. Their common feature is that both succeed in fully incorporating the slow-mode contributions to $\mathrm{Re}[\mathcal{G}^{\rm bath}(0)]$. For the CFE this is guaranteed by construction. For GV-averaging using $|G\rangle^{\rm V}_{N_T}$, it reflects the ability of the variational MPS scheme to correctly deal with the large energy shift $\delta\varepsilon^S_{N_T}$ at the end of the length-N_T RWC.

Fifth, the other two methods fail to yield a T-independent result even for C2, since, being based on Wilsonian NRG, they fail to properly deal with the last slow shift. TW- and GW-averaging involve, respectively, a thermal average or ground-state expectation value for Wilson shell N_T; but the slow shift $\delta\varepsilon^S_{N_T}$ on the last site is so large that upon adding it to the chain, some feedback to earlier sites becomes necessary. Since Wilsonian NRG does not allow for such feedback, while a variational MPS approach does (through back and forth optimization sweeps along the chain), TW- and GW-averaging fail, whereas GV-averaging does not. We also note that GW does better (yielding a weaker T-dependence) than TW. Presumably the reason is that the thermal average used by the latter incorporates information from higher-lying Wilson states $|s\rangle^{\rm W}_{N_T}$, for which the $\omega = 0$ focus of the static approximation works less well than for the shell's ground state $|G\rangle^{\rm W}_{N_T}$.

The upshot of the above analysis is that GV-averaging fully meets the challenge of correctly computing $\chi(T)$ for the DHO. Therefore, GV-averaging was the scheme used for the VMPS calculation of $\chi(T)$ reported in Figs. 2 and 3 of the main text.

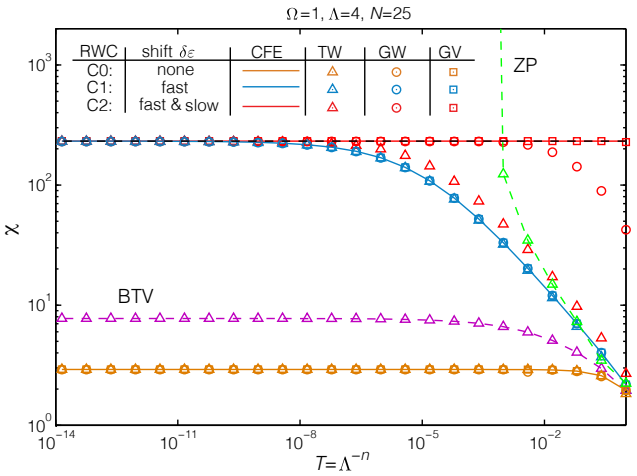

Figure S5. The static susceptibility $\chi(T)$ of the DHO as function of temperature, for $\alpha = 0.199$, $s = 0.4$. The black dashed line gives the exact result $\chi_{\rm exact}$ expected from Eq. (S30), the purple and green symbols the results obtained with standard NRG using the discretization scheme of BTV and ZP, respectively. The other data are numerical results for three types of RWC, C0 (orange), C1 (blue), and C2 (red), obtained in four different ways. The first uses a CFE of length N_T to evaluate $\mathrm{Re}[\mathcal{G}_0(0)]$ in Eq. (S30) (CFE, solid lines), while including both $\Sigma^S_n(\omega)$ and $\Sigma^F_N(\omega)$ for C2 (red), only $\Sigma^F_n(\omega)$ (blue), or neither of the two (orange). The second evaluates $\langle\ldots\rangle_T$ in Eq. (S29) as thermal average over Wilson shell N_T (TW, triangles). The other two ways approximate $\langle\ldots\rangle_T$ by an expectation value taken w.r.t. one of two different single states: the ground state $|G\rangle^{\rm W}_{N_T}$ of Wilson shell N_T (GW, circles) and the variational ground state $|G\rangle^{\rm V}_{N_T}$ of a length-N_T chain (GV, squares). In all cases, the derivative $d/d\epsilon$ in Eq. (S29) was evaluated numerically, using several ϵ-values chosen small enough (typically $\ll T$) to ensure that the calculated averages depend linearly on ϵ. TW-, GW- and GV-averages require a separate run for each combination of T and ϵ.

D. Critical ouppling $\alpha_{\rm c}$

We now turn our attention a small but very important detail illustrating the power of RWCs to minimize discretization artefacts: the determination of the critical coupling $\alpha_{\rm c}$. Its analytical value for the parameters used here is $\alpha_{\rm c} = 0.2$. Numerically, we determined $\alpha_{\rm c}$ by monitoring the divergence of the susceptibility, as described at the end of Sec. S-2 C.

On a SWC with $\Lambda = 4$, the analytical value is either largely overestimated when using the BTV discretization scheme ($\alpha_{\rm c}^{\rm BTV} \approx 0.228$), or underestimated when using the improved ZP discretization ($\alpha_{\rm c}^{\rm ZP} \approx 0.1984$); the deviations are due to the missing information of the TBMs in the Wilson chain setup. In Fig. S5, computed for $\alpha = 0.199$, this causes the low-temperature limit of the

susceptibilities χ^{BTV} and χ^{ZP} to lie far below or above the analytical value χ_{exact}, respectively. (In fact, χ^{ZP} diverges in that figure because $\alpha = 0.199$ lies above the critical coupling α_c^{ZP}.)

In contrast, the critical coupling obtained for a C2-RWC matches almost perfectly with the analytic result. For our setup, we found $\alpha_c = 0.199998$. It is possible to systematically reduce the deviation from the analytical value of α_c even further by improving the resolution of the frequency grid used to represent $\mathcal{G}_n^X(\omega)$ while constructing a RWC. Once again, this illustrates the power of our RWC construction and points out how missing TBMs can introduce systematic "discretization" artefacts. Correspondingly, we expect that RWCs will turn out to be useful for reducing discretization artefacts also for other dynamic quantities such as local spectral functions.

As α is tuned ever closer to α_c, the VMPS scheme experiences increasing convergence problems, resulting in increasing errors for $\chi(0)$. This is not surprising, because the effective potential of the DHO becomes ever shallower the nearer α approaches α_c, where the energy of one mode vanishes. That leads to very large zero-point fluctuations, and a very strong linear response to small values of ϵ. Increasing the VMPS bond dimension to keep more states during the calculation failed to significantly improve $\chi(0)$. We were able to ameliorate this convergence problem to some extent by implementing an optimized boson basis designed to incorporate large bosonic displacements. However, as a matter of principle, this problem will become unmanageable in the limit $\alpha \to \alpha_c$.

S-4. RG FLOW TOWARDS GAUSSIAN FIXED POINT

In this section, we connect the numerically obtained energy-level diagrams to analytical considerations and show that the numerical results prove the existence of a Gaussian critical fixed point for the SBM with bath exponents $0 < s \leqslant 0.5$.

Using a Feynman path-integral representation, the spin-boson model (7) can be shown to be equivalent – in the scaling limit – to the following one-dimensional ϕ^4 theory:

$$\mathcal{S} = \int \frac{d\omega}{2\pi}(m_0 + |\omega|^s)|\phi(i\omega)|^2 + \int d\tau \left[u_0\phi^4(\tau) + \bar{\epsilon}\phi(\tau)\right] \tag{S33}$$

where $\bar{\epsilon}$ is a rescaled bias, and the $|\omega|^s$ term arises from integrating out the oscillator bath with bath exponent s; this generates a bilinear coupling which is long-ranged in time. m_0 is the (bare) mass of the Ising order parameter ϕ; an increase of m_0 corresponds to a decrease in the dissipation strength α. Finally, u_0 is the quartic self-interaction. By universality arguments, the same ϕ^4 theory also describes the phase transition of a classical Ising chain with $1/r^{s+1}$ interactions.

Power counting in Eq. (S33) yields the scaling dimensions at criticality:

$$\begin{aligned} \dim[\phi(\tau)] &= (1-s)/2\,, \\ \dim[u_0] &= 1 - 4\dim[\phi(\tau)] = 2s - 1\,, \end{aligned} \tag{S34}$$

i.e., the system is above (below) its upper-critical dimension for $s < 0.5$ ($s > 0.5$).

In the following, we focus on the regime $0 < s \leqslant 0.5$ where the transition is controlled by a Gaussian fixed point. Although the quartic interaction u_0 is irrelevant at criticality, i.e., its fixed-point value is zero, it is required to stabilize the system and it influences observables in a nontrivial fashion, hence it is termed "dangerously irrelevant". The scaling dimension (S34) implies that the leading-order behavior of the dimensionless renormalized quartic coupling u, defined as $u_0 = \mu^{1-2s}u$ with μ a renormalization energy scale, at criticality is given by

$$u \propto \varepsilon_{\mathrm{uv}}^{1-2s} \tag{S35}$$

with logarithmic corrections present at s=0.5, where $\varepsilon_{\mathrm{uv}}$ is the running ultraviolet cutoff. From this we can expect that the many-body spectrum, i.e., the energy-level flow as described above, displays families of levels whose spacing goes to zero as the cutoff energy $\varepsilon_{\mathrm{uv}}$ goes to zero. This is in contrast to interacting critical fixed points, here realized for $0.5 < s < 1$ where the renormalized u reaches a finite fixed-point value: This causes the level spacings to approach constant values as $\varepsilon_{\mathrm{uv}} \to 0$ (see Ref. 41 for a detailed analysis of NRG fixed-point spectra at interacting critical points). Both behaviors are nicely borne out by our numerical results in Figs. 4 and S6.

While the effect of u on many observables can be calculated using (renormalized) perturbation theory, this does not apply to the level spectrum at criticality: For $u = 0$ the spectrum is degenerate (reflecting a bosonic zero mode), such that the effect of u is nonperturbative. This zero-mode physics in the presence of a quartic interaction is captured by the toy-model Hamiltonian for a quartic oscillator, $\mathcal{H}_4 = p^2/(2m) + ux^4$ in standard

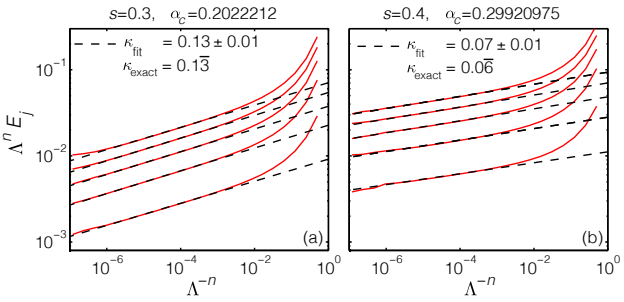

Figure S6. Energy-level flow diagram for the SBM on a C2-RWC obtained for (a) $s = 0.3$ and (b) $s = 0.4$ at the critical point. The dashed lines illustrate the power-law fits employed to extract the exponent κ characterizing the Gaussian fixed point. The numerical results are in excellent agreement with the analytical prediction $\kappa = (1-2s)/3$.

notation. Scaling considerations shows that the eigenenergies of this model obey the exact scaling $e_i \propto u^{1/3}$. Importantly, this toy model, if used with a renormalized u, describes *renormalized* energy levels.

Let us now connect the behavior of these renormalized energy levels with those generated by NRG. To this end, we note that in NRG the Wilsonian scale $\varepsilon_n \propto \Lambda^{-n}$, which is an infrared cutoff, controls the RG flow in a way analogous to that of the running UV cutoff $\varepsilon_{\mathrm{uv}}$ in a perturbative RG scheme, as both schemes are designed to describe the renormalized physics at the scale $\varepsilon_{\mathrm{uv}}$. Indeed, in an NRG calculation the ultraviolet cutoff at a fixed point is a multiple of the infrared cutoff ε_n. Combining the energy scaling of $\mathcal{H}_4$ with Eq. (S35), we conclude that the low-lying renormalized energy levels obtained from mVMPS, $\Lambda^n E_j$, scale with the Wilsonian energy scale $\varepsilon_n \propto \Lambda^{-n}$ as

$$\Lambda^n E_j \propto \left(\Lambda^{-n}\right)^{\kappa} \text{ with } \kappa = (1-2s)/3\,, \tag{S36}$$

characterizing the approach to a Gaussian fixed point. Fig. S6 shows a log-log plot of the energy-level flow for two values of s, together with a power-law fit. We obtain $\kappa = 0.13 \pm 0.01$ for $s = 0.3$ and $\kappa = 0.07 \pm 0.01$ for $s = 0.4$, in excellent agreement with the analytical prediction, which yields $0.4/3 = 0.1\bar{3}$ and $0.2/3 = 0.0\bar{6}$, respectively.